

Explosive hydrogen burning during type I X-ray bursts

Jacob Lund Fisker

Department of Physics and Joint Institute for Nuclear Astrophysics, University of Notre Dame, Notre Dame, IN 46566, USA

jfisker@nd.edu

Hendrik Schatz

Department of Physics and Astronomy and National Superconducting Cyclotron Laboratory and Joint Institute for Nuclear Astrophysics, Michigan State University, East Lansing, MI 48824-2320

schatz@nscl.msu.edu

Friedrich-Karl Thielemann

Department of Physics and Astronomy, University of Basel, Klingelbergstrasse 82, 4056 Basel, Switzerland

F-K.Thielemann@unibas.ch

ABSTRACT

Explosive hydrogen burning in type I X-ray bursts (XRBs) comprise charged particle reactions creating isotopes with masses up to $A \sim 100$. Since charged particle reactions in a stellar environment are very temperature sensitive, we use a realistic time-dependent general relativistic and self-consistent model of type I x-ray bursts to provide accurate values of the burst temperatures and densities. This allows a detailed and accurate time-dependent identification of the reaction flow from the surface layers through the convective region and the ignition region to the neutron star ocean. Using this, we determine the relative importance of specific nuclear reactions in the X-ray burst.

Subject headings: X-rays: bursts — nuclear reactions, nucleosynthesis, abundances — stars: neutron

1. Introduction

Type I X-ray Bursts (XRBs) (see Bildsten (1998); Strohmayer & Bildsten (2006) for reviews) were first explained by Woosley & Taam (1976) who associated the XRBs with thermonuclear runaways on the surface of neutron stars that accrete a mixture of hydrogen and helium from a semi-detached low mass companion star (Joss 1977).

In Woosley & Taam’s *thermonuclear flash model* the impact of the accreting matter fully ionizes the matter and heats it to $1 - 2 \times 10^8$ K explaining the persistently observed X-ray emissions. The accreted matter then undergoes gradual compression as it sinks as new matter continuously piles on top of it. Under these atmospheric conditions the electrons are degenerate, but the nucleons are not. Therefore the matter is subject to a thin-shell instability that triggers a thermonuclear runaway (Hansen & van Horn 1975). For accretion rates below roughly one Eddington ($\dot{M} = 1.12 \times 10^{18} \text{ g s}^{-1}$), the bottom layer of the newly accreted matter becomes unstable after a few hours/days and burns explosively and gives rise to a burst of X-rays as the atmosphere is heated to 1-1.5 GK. The sudden release of nuclear binding energy heats the atmosphere rapidly and increases the luminosity within a few seconds after which the luminosity decays exponentially as the atmosphere cools again producing the observational features of a type I X-ray burst (Joss 1978; Taam 1980). These bursts are the most common thermonuclear explosions in the universe, so the indestructable and repeatable LMXBs are useful for indirect conclusions about the behavior of matter under extreme conditions.

X-ray bursts have been explored theoretically by Hanawa & Sugimoto (1983); Fujimoto et al. (1987); Koike et al. (1999) and stable burning has been explored by Schatz et al. (1999) using relatively simple hydrodynamical models to estimate the burning conditions e.g. a set of (ρ, T, \vec{X}) , where ρ is the density, T is the temperature, and \vec{X} is a composition array describing the fractional concentration of each isotope. On the other hand more realistic 1 dimensional models have been constructed by many groups (Joss 1978; Taam & Picklum 1979; Hanawa & Sugimoto 1983; Wallace et al. 1982; Ayasli & Joss 1982) but they suffered from relatively simple nuclear reaction networks so only recently models have successfully included both aspects (Woosley et al. 2004; Fisker et al. 2004, 2006).

The relevant types of reaction sequences in XRBs have been discussed by Wallace & Woosley (1981); Champagne & Wiescher (1992); van Wormer et al. (1994); Herndl et al. (1995); Schatz et al. (1998); Schatz & Rehm (2006). Important are (p, γ) -, (α, γ) -, (p, α) -reaction rates as well as β -decay rates between the valley of stability and the proton dripline. Reaction rates must be known up to the end-point of the *rp*-process (Schatz et al. 2001a).

In the past several attempts have been made to identify critical reaction rates in X-

ray bursts. It is, however, not possible to directly test the astronomical number of possible perturbations of the thousands of participating reaction rates. Woosley et al. (2004) changed groups of decay rates and narrowed the rates down to several important candidates. Fisker (2004); Fisker et al. (2004, 2006) relied on “inspired guesses” and found individual important rates. Recently, Amthor et al. (2006) has used a one-zone model and individually varied a large number of reaction rates with the intent of verifying “one-zone”-candidates with a multi-zone model. Using Monte Carlo methods, Roberts et al. (2006) varied random groups of reaction rates and similarly identified the most significant candidates for later verification with multi-zone models.

In this paper, we use such a full 1D X-ray burst model with a complete nuclear reaction network to answer one of the fundamental questions in this field: what are the nuclear reactions that power X-ray bursts? While previous studies have used simplified models to delineate basic types of reaction sequences we can now go the next step and describe the actual nuclear reaction sequences that occur as a function of time and depth during a typical X-ray burst. Because temperature, density, and initial composition vary greatly as a function of depth there is no single reaction flow, but a range of very different sequences that influence each other. Identifying the nuclear reactions that take place in X-ray bursts is a prerequisite for understanding X-ray burst light curve features in terms of the underlying nuclear physics and for determining the nuclear physics uncertainties in X-ray burst model predictions of lightcurves and other observables. It is also essential to guide experimental and theoretical efforts to address these uncertainties in the future.

Cross sections have typically been predicted by global models which in most cases have been fitted to stable nuclei and extrapolated to proton-rich nuclei. In many cases cross sections have also been predicted by nuclear shell model calculations. However, with upgrades of existing experimental facilities and new facilities many of these reactions are now in range of experiments (Käppeler et al. 1998; Wiescher 2001; Wiescher & Schatz 2001; Schatz 2002).

With a better understanding of the nuclear physics it will also become possible to address potential issues beyond the 1D approximation, such as the interplay of lateral flame propagation and nuclear energy release timescales that can affect the modeling of burst rise times.

2. The 1D multi-zone computational burst model

In this paper we compute and describe one XRB model using the parameters $M = 1.4M_{\odot}$, $R = 11\text{km}$ and a proper global accretion rate of $\dot{M} = 1 \cdot 10^{17}\text{g/s}$. This choice

yields a H/He-ignited XRB corresponding to case (1) of Fujimoto et al. (1981) where the observational data depends more on the *rp*-process than is the case for a pure He-ignited XRB (case (2) of Fujimoto et al. (1981)). The Newtonian accretion rate (observable at infinity) of Schatz et al. (2001a,b) and model zM of Woosley et al. (2004) was $\dot{M} = 5 \cdot 10^{16} \text{ g s}^{-1}$, so the burst behavior of our model is expected to be similar but have a slightly higher hydrogen content and a slightly lower helium content at the point of ignition resulting in a longer rise time.

This model is calculated using a general relativistic type I X-ray burst simulation code that is described in more detail in Fisker et al. (2006). The code couples the general relativistic hydrodynamics code, **AGILE** (Liebendörfer et al. 2002), with the nuclear reaction network solver of Hix & Thielemann (1999). The code includes radiative, conductive, and convective heat transport as described in Thorne (1977) and uses an arbitrarily relativistic and arbitrarily degenerate equation of state. We calculate the radiative opacities due to Thomson scattering and free-free absorption using the analytic formulations of Schatz et al. (1999). We use the same conductivity formulations for electron scattering on electrons, ions, phonons, and impurities as Brown (2000).

AGILE solves the general relativistic equations in a spherically symmetric geometry on a comoving grid. The computational domain covers about 7 pressure scale heights and is discretized into 129 log-ratioed grid zones with a column density¹ ranging from $y = 1.2 \times 10^6 \text{ g cm}^{-2}$ to $y = 3.9 \times 10^9 \text{ g cm}^{-2}$. The computational domain is bounded by a realistic core boundary interface (Brown 2003, 2004) and a relativistically corrected grey atmosphere (Thorne 1977; Weiss et al. 2004) which is integrated numerically out to $P_{surf} = 10^{18} \text{ g cm}^{-2}$ using a 4th order Runge-Kutta method for greater accuracy (Fisker et al. 2006).

The *rp*-process is naturally limited once it reaches the $A \sim 104$ region because neutron deficient nuclei in this mass range become α -unbound. This terminates the reaction flow via (γ, α) reactions and forms a SnSbTe cycle (Schatz et al. 2001a). This determines the maximum network size that is needed, unless the alpha unbound nuclei can be circumvented in multiple proton exposures. Schatz et al. (2001a) demonstrated that the $A \sim 104$ endpoint can be reached if burst peak temperatures and hydrogen concentration at ignition are high. However, Woosley et al. (2004) showed, that these ignition conditions are only fulfilled for the first burst after the start of accretion on a pure ^{56}Fe atmosphere. Compositional inertia effects (Taam 1993) for subsequent bursts significantly reduce peak temperature and the

¹ The relativistic column density is mass of a column above an area: $y \equiv \int_{R-r}^R \rho \frac{dr}{\Gamma}$ where $\Gamma = \sqrt{1 - 2GM/Rc^2}$, so $P \simeq gy$, where R is the neutron star radius, M is the neutron star mass, ρ is the density, P is the pressure, and $g = GM/\Gamma R^2$ is the surface acceleration of gravity.

amount of hydrogen at ignition as ignition occurs at a lower pressure and depth thus limiting the rp-process to $A \lesssim 64$ with only a fraction of heavier isotopes produced.

The nuclear reaction network used in this work employs 304 isotopes (see table [1]). All the connecting particle reactions are taken from the REACLIB (see Sakharuk et al. (2006)). These reaction rates have also been used in Weinberg et al. (2006). The network includes all isotopes between the valley of stability and the proton dripline up to ^{64}Ge . Here isotopes with β^+ -half lives > 1 day are considered “stable” on the timescale of the burst intervals, so their daughters are not included. The hot proton-proton chains of Wiescher et al. (1989) are also included. Above the ^{64}Ge waiting point, only isotopes between the proton drip line and half lives less than 1 minute are included. This is because protons only capture on these high- Z isotopes during the burst’s peak temperature which is only sustained for a few seconds. Weak rates up to $Z = 32$ are taken from Fuller et al. (1980, 1982a,b) and Langanke & Martínez-Pinedo (2001). Since only a small fraction of material is processed above $Z = 32$, it is a reasonable approximation to ignore neutrino losses from heavier isotopes (Schatz et al. 1999). These considerations significantly reduce the size of the network which decreases the simulation run-time. The inner boundary, i.e. towards the neutron star crust, has been slightly improved compared to previous work which used either a massive substrate (Woosley et al. (2004)) or parameter values (Rembges (1999)). This work uses the neutron star core code of Brown (2000, 2003) which calculates the thermal luminosity emanating from the crust given the temperature at the atmosphere-ocean interface. The code includes pair, photo, and plasmon neutrino emission. This neutrino luminosity is only a few percent of the thermal luminosity but still several orders of magnitude larger than the hydrodynamical uncertainty due to the conservative formulation of mechanical equations. Different types of convection occur when thermal fluctuations cause instabilities to grow. Their rate of growth determine the eddy-velocity, so all instabilities can be treated by the mixing length theory (MLT) implementation. The present work only includes the Schwarzschild-Ledoux instability, because it is the dominant form of convection during the burst (which is the only period relevant to this paper), whereas secular instabilities (e.g. semi-convection) occur in between bursts and are negligible at high accretion rates, because the diffusion speed is smaller than the advection speed of the accretion. The initial model was computed by running the simulation for hundreds of bursts until the burst ashes had advected completely to the bottom of the model and the computational envelope was in thermal balance with the neutron star core model. At this point, the envelope was considered to be self-consistent, that is, independent of any possibly unphysical initial values, and a typical X-ray burst was picked for analysis.

Z	A	Z	A	Z	A
n	1	Ar	31–38	Kr	69–74
H	1–3	K	35–39	Rb	73–77
He	3,4	Ca	36–44	Sr	74–78
Li	7	Sc	39–45	Y	77–82
Be	7,8	Ti	40–47	Zr	78–83
B	8,11	V	43–49	Nb	81–85
C	9,11,12	Cr	44–52	Mo	82–86
N	12–15	Mn	47–53	Tc	85–88
O	13–18	Fe	48–56	Ru	86–91
F	17–19	Co	51–57	Rh	89–93
Ne	18–21	Ni	52–62	Pd	90–94
Na	20–23	Cu	54–63	Ag	94–98
Mg	21–25	Zn	55–66	Cd	95–99
Al	22–27	Ga	59–67	In	98–104
Si	24–30	Ge	60–68	Sn	99–105
P	26–31	As	64–69	Sb	106
S	27–34	Se	65–72	Te	107
Cl	30–35	Br	68–73		

Table 1: The table shows the list of isotopes which describes the *rp*-process. See the main text for details. An earlier version of this reaction network has been used in the following works (Fisker 2004; Fisker et al. 2004, 2005a,b, 2006) but it now includes the hot proton-proton chains of Wiescher et al. (1989). The network is described in more detail in Fisker et al. (2006).

3. Burst simulations

Fig. 1 shows the luminosity for the analyzed burst as a function of time. When comparing it to observations, it should be kept in mind that our model assumes a spherical symmetric ignition whereas in reality ignition most likely happens at a single point on the neutron star after which the flamefront spreads and eventually covers the entire neutron star. Therefore Fig. 1 may be thought of as the luminosity of a single point under the assumption of negligible lateral heat transport. However, this assumption seems to provide a good comparison to reality (Galloway et al. 2004).

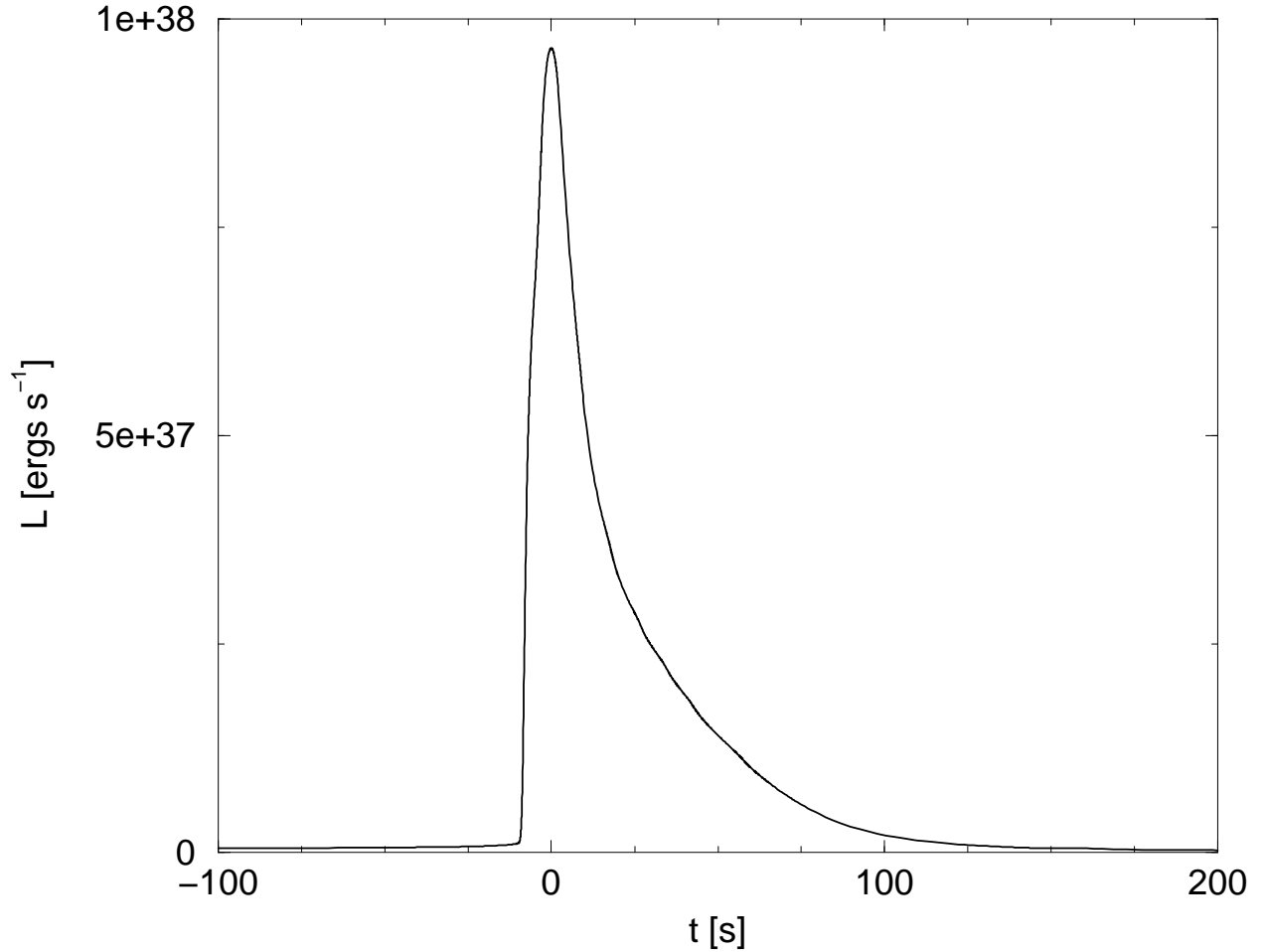


Fig. 1.— The figure shows the luminosity as seen from an observer at infinity as a function of time for a typical burst. The timescale has been reset so that $t = 0$ corresponds to the peak luminosity of the burst.

The luminosity is the combined product of the energy released from nuclear reactions at different depths. The Kippenhahn diagram in Fig. 2 shows the specific nuclear energy release rate as a function of column density and time as well as the extent of the convective zone.

The ignition region is easily identified as a sudden and rapid increase in nuclear energy generation. This causes a temperature spike that causes a convective instability. Since convection transports heat very efficiently, the zones above the ignition point also ignite. This is clearly seen in Fig. 2. However, this heat transport quickly restores the shallower radiative/conductive temperature gradient and convection quickly ends. The Kippenhahn diagram also demonstrates how nuclear energy generation decreases as fuel depletes and how residual helium from the previous burst contributes to nuclear reactions below the ignition region. Still, most of the nuclear energy is released, not at the point of ignition but in the hydrogen rich layers immediately above the ignition region.

4. Reaction flow

Runaways occurring in a mixed H/He layer mainly proceed via the *rp*-process (Wallace & Woosley (1981)), where the characteristic timescale, $\tau_{rp} \sim \sum T_{1/2}$, is given by the sum of the half-lives of the β -decays in the reaction flow (van Wormer et al. (1994)). However, depending on the flow pattern, a simultaneously occurring (α, p)-process, which does not depend on β -decays, may decrease the timescale through the *sd*-shell nuclei (Wallace & Woosley (1981); Schatz et al. (1998); Fisker et al. (2004)). As the runaway lasts several seconds for a H/He-ignited XRB, the temperature gradient only produces a minor convective instability.

The analysis of a one-dimensional X-ray burst model is very complex, as the model is characterized by rapidly changing temperature conditions and nuclear reaction sequences in each layer. All these effects are tightly interconnected through energy generation and heat transport by radiation and convection. Since the different layers interact and also burn differently due to different compositions and temperature, the burst can not be understood based on the burning of one layer only, but must be analyzed for several different burning layers. Therefore the analysis is split into four regions: the region around the ignition point, the convective region, the surface, and the ocean, which are sufficiently different to merit separate attention. These regions are shown in Fig. 3 which shows a trace of the burst conditions for different depths (pressures) during a complete revolution of the limit cycle.

Following the cooling of the previous burst, the individual layers reach their lowest temperature and highest density of the cycle. The subsequent accretion increases the hy-

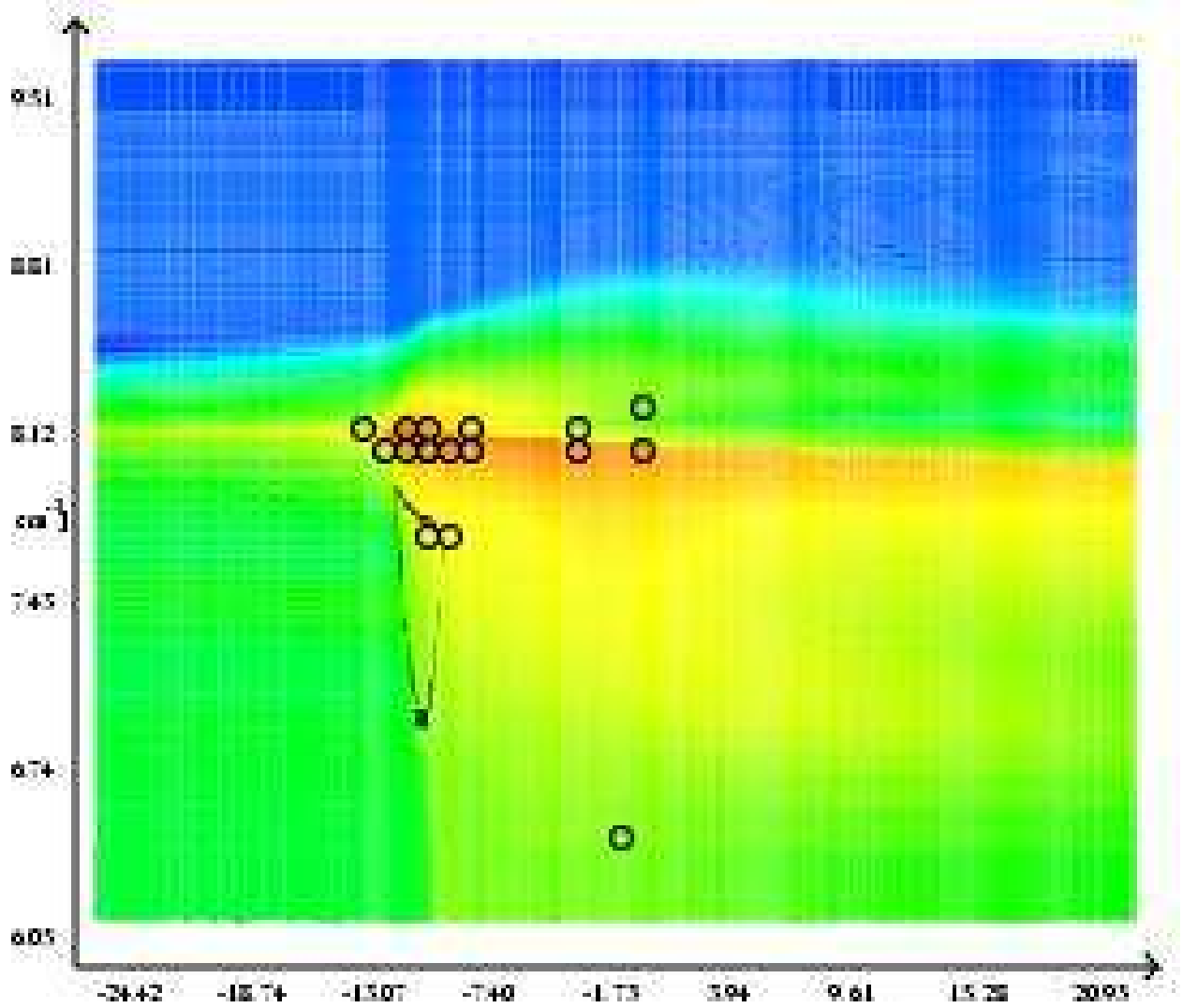


Fig. 2.— The figure shows the specific nuclear energy release rate (color coded) as a function of logarithmic (\log_{10}) relativistic column density (see footnote 1) and time as well as the extent of the convective zone (black sail shaped outline). The black circles correspond to the descriptions of the reaction flow in §4. Starting from the top of the figure, they are: ocean (4.5), ignition region (4.1.2–4.1.6, 4.1.1 is not shown), above ignition region (4.2.2–4.2.9), 4.2.1 and 4.2.10 are not shown), bottom of the convective region (4.3.1–4.3.2), and surface (4.4.1).

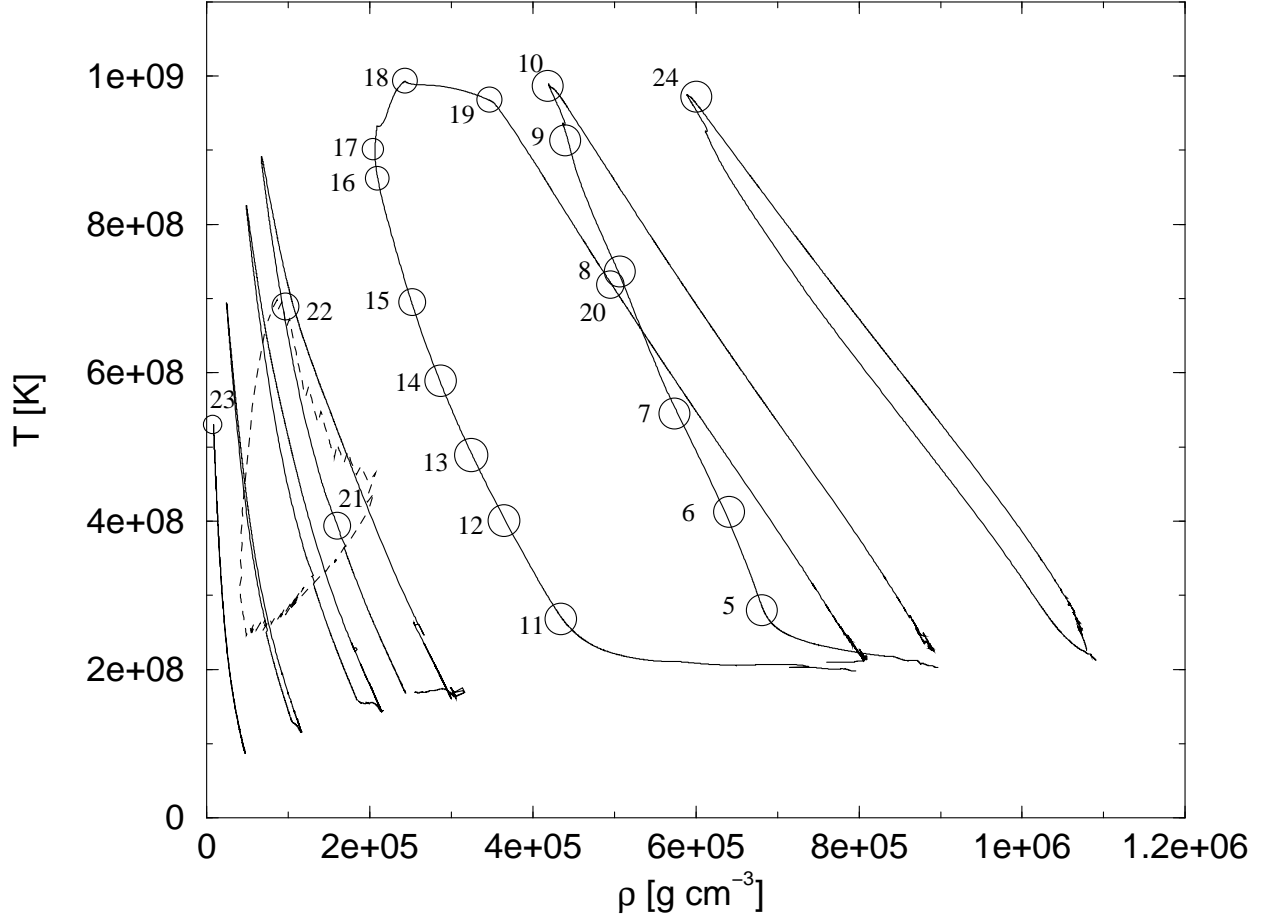


Fig. 3.— From left to right (solid line): $y = 1.8 \times 10^6 \text{g/cm}^2$ (surface), $y = 1.0 \times 10^7 \text{g/cm}^2$ (top of the convective region), $y = 2.5 \times 10^7 \text{g/cm}^2$, $y = 3.7 \times 10^7 \text{g/cm}^2$ (bottom of the convective region), $y = 7.9 \times 10^7 \text{g/cm}^2$ (above ignition), $y = 9.5 \times 10^7 \text{g/cm}^2$ (ignition point), and $y = 1.2 \times 10^8 \text{g/cm}^2$ (ocean). The dashed line indicate the region which is convective during the rising of the burst. The circles and their associated numbers correspond to the figures in §4.

drogen content of the layer, which in turn lowers the density, because the increased electron abundance of hydrogen requires less mass to maintain the hydrostatic pressure (Joss (1977); Joss & Li (1980)) compared to the heavier and more neutron-rich ashes (Hanawa & Fujimoto (1984)). This is most clearly seen in Fig. 3 just above the ignition region, which decreases its density by about a factor two during the quiescent phase, as the electron-rich surface ashes of the previous burst sink into this region. For an accretion rate of $\dot{M} = 1 \cdot 10^{17} \text{g/s}$ and a recurrence time of $\Delta t \approx 11000 \text{s}$, the neutron star accretes a mass of $\Delta M = \dot{M} \cdot \Delta t \approx 1.1 \cdot 10^{21} \text{g}$ ($5.5 \cdot 10^{-13} M_{\odot}$) in between bursts. This means that matter above $y = 5.8 \times 10^7 \text{g/cm}^2$ is freshly accreted, whereas matter below comprise the old surface ashes of the previous burst(s), therefore the composition in the ignition region actually consist of heavier ashes with a comparably lower hydrogen/helium abundance. When the matter ignites and the nuclear runaway causes a rising temperature, it eventually affects the degeneracy of the electrons and decreases the density further so the trace runs up the left leg of the cycle in Fig. 3 until the fuel is exhausted as it burns into heavier ashes shortly after the peak temperature is reached. The β^+ -decays during and subsequent to the rp -process decrease the electron abundance and bring the trace down the right leg as the envelope cools. Therefore the separation in density between the rising leg and the decaying leg accounts for the change in composition, so the largest change happens around the ignition regions, whereas the surface does not change its composition much. The different compositions and hydrostatic pressures with corresponding temperatures and densities of the burning regions change dynamically on a nuclear timescale defined as $\min(dt/d \ln Y_i)$, where Y_i is the abundance of the i th isotope. Therefore the analysis of the nuclear reaction flow proceeds in a different way compared to previous works, which assumed solar abundances burning at fixed densities and temperatures and described the integrated flow over many minutes (van Wormer et al. (1994); Rembges et al. (1997)); instead the instant flow rate is described as the thermodynamic state variables change.

The net reaction flow rate from isotope i to isotope j is defined by

$$f_{ij} = -f_{ji} = \dot{Y}_{i \rightarrow j} - \dot{Y}_{j \rightarrow i}, \quad (1)$$

where $\dot{Y}_{i \rightarrow j}$ is the time rate-of-change of the abundance of the i th isotope resulting from all reactions converting isotope i to isotope j . The flow-rates for the different times of Fig. 3 will be demonstrated in the flowcharts of the following sections, which describe the reaction flow rates at the ignition point, the region above it, the convective zone, the surface (of our model), and the ashes going into the ocean.

In these figures the main reaction-flow is described by the heavy lines. Very thick lines indicate $(p, \gamma)(\gamma, p)$ -equilibrium. Thin lines indicate a flow rate just above 10^{-6}mol/g/s increasing their thickness logarithmically to a maximum after which they stay constant. Also

shown are the mass fractions, $X_A = \sum_{A_i=A} X_i$, for a given mass, A , as a function of mass number. If $X_A > 0.20$ for any A , the bar is cut off and replaced with a dotted line. This only happens for the $A = 1$ and $A = 4$ cases where the concentration can be read in the figure caption.

4.1. Ignition region

Between bursts, the surface ashes from the previous burst sink down under the weight of the newly accreting matter while the hot CNO cycle transforms hydrogen into helium. The hot CNO cycle is beta-limited and therefore burns at a fixed rate that mainly depends on the concentration of ^{14}O and ^{15}O . It is partially moderated by a quiescent breakout via the $^{15}\text{O}(\alpha, \gamma)^{19}\text{Ne}$ reaction which depletes ^{15}O and thus slows down the conversion of hydrogen into helium. This is discussed in more detail in Fisker et al. (2006). As seen in figure 5, the reaction flow can subsequently return to the hot CNO cycle via the bi-cycle $^{19}\text{Ne}(\beta^+ \nu)^{19}\text{F}(p, \alpha)^{16}\text{O}(p, \gamma)^{17}\text{F}(p, \gamma)^{18}\text{Ne}(\beta^+, \nu)^{18}\text{F}(p, \alpha)^{15}\text{O}$ which speeds up the conversion of hydrogen to helium and thus influences the composition for the runaway. This cycle is discussed in more detail in Cooper & Narayan (2006).

The hot CNO cycle increases the ^4He concentration until a runaway of the extremely temperature sensitive triple-alpha reaction ensues and causes a spike in the nuclear energy release rate.

The triple-alpha reaction creates ^{12}C which immediately captures two protons to become ^{14}O , causing the fraction of ^{14}O ($T_{1/2} = 76.4\text{s}$) to increase as seen in Fig. 4, since ^{14}O ($T_{1/2} = 76.4\text{s}$) decays too slowly. Meanwhile the increasing temperature of the nascent nuclear runaway leads to a breakout of the hot CNO cycle into the *rp*-process. The details are described in the following subsections.

We now describe the reaction flow in terms of temperature, density, and proton and alpha fractions as the time develops. The time is synchronized, so $t = 0$ coincides with the peak surface luminosity.

4.1.1. Fig. 5: $T = 2.86 \cdot 10^8\text{K}$, $\rho = 6.81 \cdot 10^5\text{g/cm}^3$, $X = 0.09$, $Y = 0.42$, $t = -103.078\text{s}$

At this time the increasing temperature has caused the flow rate of $^{15}\text{O}(\alpha, \gamma)^{19}\text{Ne}$ (see Fisker et al. (2006) for a detailed discussion of this rate) to reach 10% of the $^{15}\text{O}(\beta^+, \nu)^{15}\text{N}$ rate establishing a breakout of the hot CNO cycle (the 1% limit was breached at $t = -558\text{s}$) which extends into the light iron region.

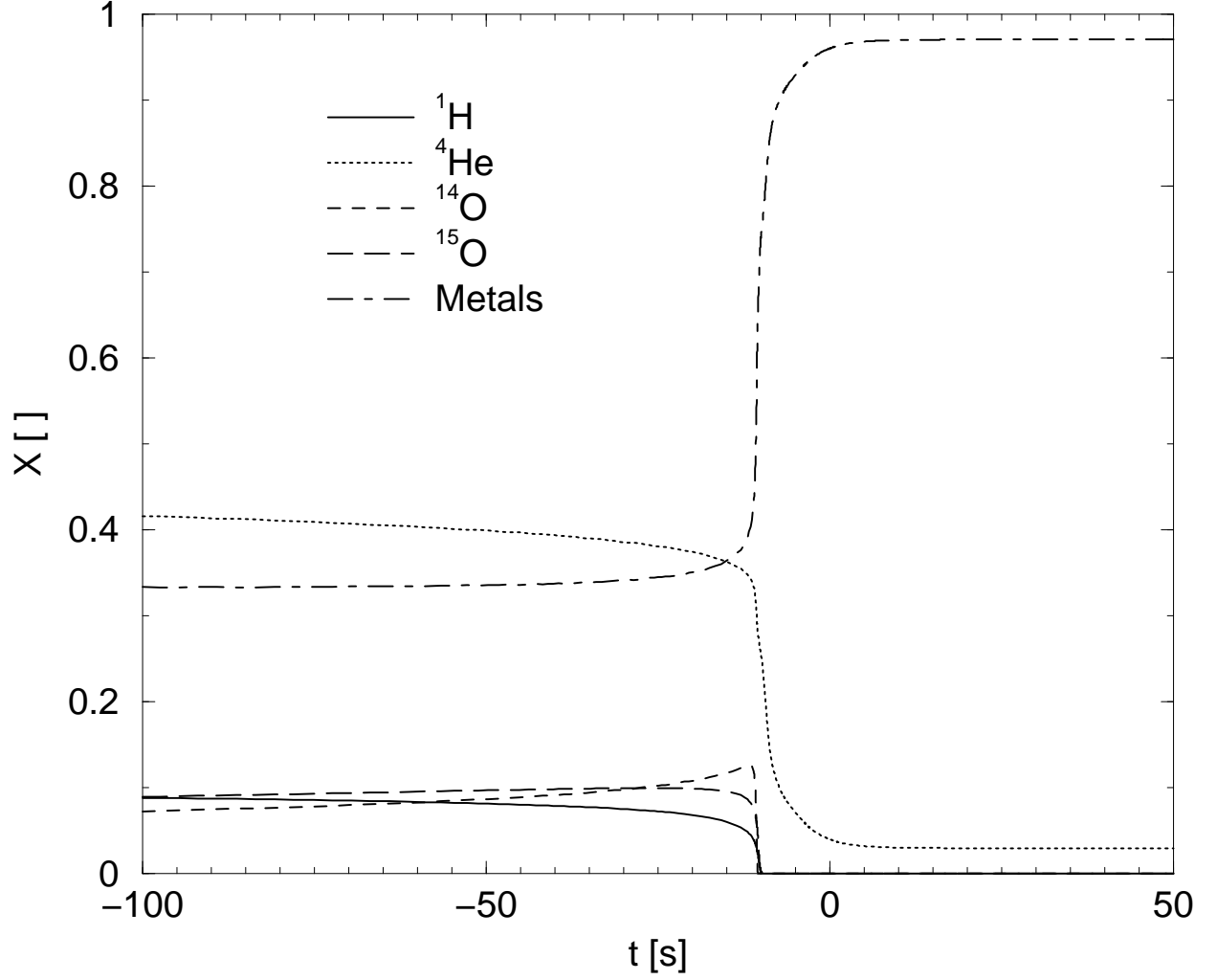


Fig. 4.— The hydrogen, helium, CNO type matter, and metal (the rest) mass fractions as a function of time. The time scale has been synchronized to coincide with the burst luminosity peak at $t = 0$. Notice the run-up in ^{14}O immediately prior to the runaway. Also note that the hydrogen in the ignition region is completely exhausted during the burst, while about $\sim 5\%$ helium remains.

At this point proton captures establish a flow out of ^{19}Ne . The matter in this flow can no longer return to the hot CNO cycle and the reaction flow proceeds with $^{19}\text{Ne}(p, \gamma) ^{20}\text{Na}(p, \gamma) ^{21}\text{Mg}$, where it is blocked by photodisintegration, because of the $^{21}\text{Mg}(p, \gamma)(\gamma, p)^{22}\text{Al}$ -equilibrium. Therefore the flow proceeds via $^{21}\text{Mg}(\beta^+, \nu)$ ($T_{1/2} = 0.124\text{s}$) $^{21}\text{Na}(p, \gamma) ^{22}\text{Mg}(\beta^+, \nu)$ ($T_{1/2} = 3.32\text{s}$) $^{22}\text{Na}(p, \gamma) ^{23}\text{Mg}(p, \gamma) ^{24}\text{Al}(p, \gamma) ^{25}\text{Si}$.

Here the flow branches into either $^{25}\text{Si}(\beta^+, \nu)$ ($T_{1/2} = 0.198\text{s}$) $^{25}\text{Al}(p, \gamma) ^{26}\text{Si}$ ($T_{1/2} = 1.84\text{s}$) $(p, \gamma) ^{27}\text{P}$ or $^{25}\text{Si}(p, \gamma) ^{26}\text{P}(\beta^+, \nu)$ ($T_{1/2} = 0.020\text{s}$) $^{26}\text{Si}(p, \gamma) ^{27}\text{P}$ or $^{25}\text{Si}(p, \gamma) ^{26}\text{P}(p, \gamma) ^{27}\text{S}(\beta^+, \nu) ^{27}\text{P}$ all of which have ^{27}P as the end point. The characteristic time depends on the mass fraction weighed harmonic mean of the half lives of the beta decays along respective pathways. As the temperature rises, the proton capture branches become initially more dominant but then decrease again as photodisintegration of the weakly proton bound and short lived proton-rich P and S isotopes steers the flow away from the dripline again. Yet at this particular temperature the beta decay path of ^{25}Si dominates the proton capture to ^{26}P .

From this point, $^{27}\text{P}(\beta^+, \nu)$ ($T_{1/2} = 0.242\text{s}$) $^{27}\text{Si}(p, \gamma) ^{28}\text{P}(p, \gamma) ^{29}\text{S}(\beta^+, \nu)$ ($T_{1/2} = 0.146\text{s}$) $^{29}\text{P}(p, \gamma) ^{30}\text{S}$ which has a half life of 1.07s. The Q -value of proton capture on ^{30}S is only 290.6keV which makes ^{31}Cl subject to photodisintegration at higher temperatures. At later times, this can have a large effect on the observed luminosity of the burst (Fisker et al. 2004).

Here, the proton capture still dominates, so the flow proceeds via $^{30}\text{S}(p, \gamma)$ ($T_{1/2} = 1.07\text{s}$) $^{31}\text{Cl}(\beta^+, \nu)$ ($T_{1/2} = 0.270\text{s}$) ^{31}S . This ($T_{1/2} = 2.13\text{s}$) isotope either beta decays and returns to ^{28}Si via $^{31}\text{P}(p, \alpha) ^{28}\text{Si}$ or captures a proton and proceeds via $^{31}\text{S}(p, \gamma)$ (Iliadis et al. (1999)) $^{32}\text{Cl}(\beta^+, \nu)$ ($T_{1/2} = 0.285\text{s}$) $^{32}\text{S}(p, \gamma) ^{33}\text{Cl}(p, \gamma) ^{34}\text{Ar}(\beta^+, \nu)$ ($T_{1/2} = 0.811\text{s}$) $^{34}\text{Cl}(p, \gamma) ^{35}\text{Ar}(p, \gamma)$ (Iliadis et al. (1999)) $^{36}\text{K}(\beta^+, \nu)$ ($T_{1/2} = 0.302\text{s}$) $^{36}\text{Ar}(p, \gamma) ^{37}\text{K}(p, \gamma) ^{38}\text{Ca}$.

Since ^{39}Sc and ^{40}Sc are almost proton unbound the flow must wait for ^{38}Ca ($T_{1/2} = 0.416\text{s}$) and ^{39}Ca ($T_{1/2} = 0.799\text{s}$) to β^+ -decay before the flow stops at the well-bound ^{40}Ca isotope. A CaScTi cycle exists on the well-bound ^{40}Ca so that $^{40}\text{Ca}(p, \gamma) ^{41}\text{Sc}(p, \gamma) ^{42}\text{Ti}(\beta^+, \nu)$ ($T_{1/2} = 0.189\text{s}$) $^{42}\text{Sc}(p, \gamma) ^{43}\text{Ti}(\beta^+, \nu)$ ($T_{1/2} = 0.429\text{s}$) $^{43}\text{Sc}(p, \alpha) ^{40}\text{Ca}$. The breakout from this cycle happens from ^{43}Sc which proceeds to capture protons going through ^{44}Ti and ^{45}V until it ends at ^{52}Fe .

The total timescale for this sequence is (c.f. van Wormer et al. (1994)) $\tau = \ln(2)^{-1} \sum T_{1/2} \sim 8\text{s}$, which is slower than the time it takes to cover the star with a deflagration wave by a factor four (Fryxell & Woosley 1982). Therefore a one-dimensional approximation is still reasonable. Later when the (α, p) -process ignites and the temperature increases, the reaction flow will move closer to the dripline decreasing the β -half-lives, thus making the timescales comparable. At that point, our model is no longer fully predictive of hydrodynamically in-

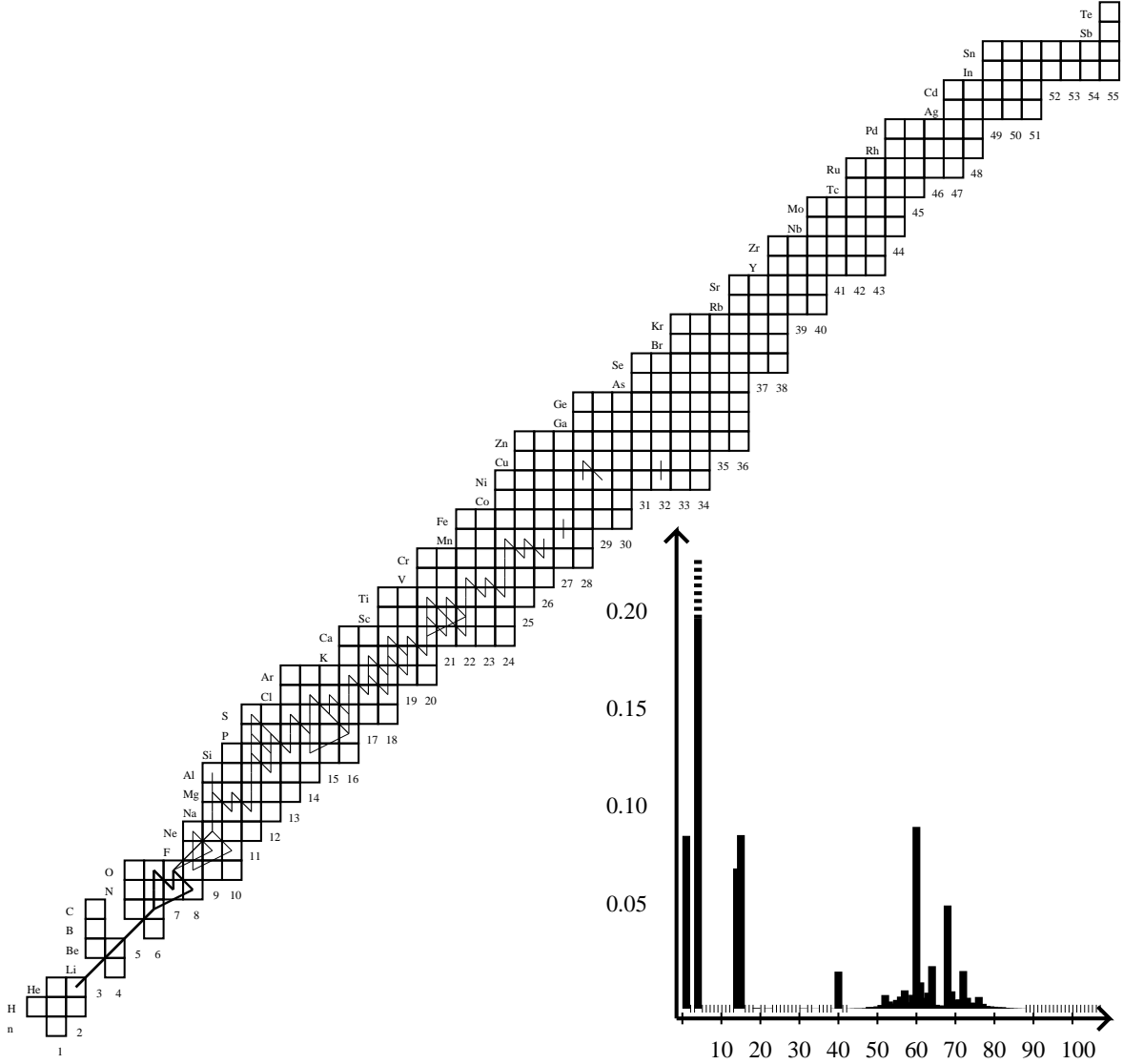


Fig. 5.— Ignition: $T = 2.86 \cdot 10^8 \text{K}$, $\rho = 6.81 \cdot 10^5 \text{g/cm}^3$, $X = 0.09$, $Y = 0.42$, $t = -103.078 \text{s}$. (see end of §4 for an explanation of the diagram).

fluenced (extensive) observables such as the time-dependent luminosity. However, our model still provides a local (intensive) description of the burning conditions, and therefore a realistic description of the reaction flow.

4.1.2. *Fig. 6:* $T = 3.99 \cdot 10^8 K$, $\rho = 6.41 \cdot 10^5 g/cm^3$, $X = 0.05$, $Y = 0.36$, $t = -12.938s$

Approximately 90 seconds later the $^{14}O(\alpha, p)^{17}F$ reaction reaches 1/3 of the flow rate of the $^{15}O(\alpha, \gamma)^{19}Ne$ -reaction. This starts a second hot CNO bi-cycle: $^{14}O(\alpha, p)^{17}F(p, \gamma)^{18}Ne(\beta^+, \nu)^{18}F(p, \alpha)^{15}O$ which runs alongside the bi-cycle discussed above in §4.1.

At this stage $^{22}Mg(p, \gamma)^{23}Al$ and $^{22}Mg(\beta^+, \nu)$ ($T_{1/2} = 3.34s$) ^{22}Na become comparable. Consequently the flow path through $^{22}Mg(p, \gamma)^{23}Al(p, \gamma)^{24}Si(\beta^+, \nu)$ ($T_{1/2} = 0.190s$) ^{24}Al competes with $^{22}Mg(\beta^+, \nu)$ ($T_{1/2} = 3.34s$) $^{22}Na(p, \gamma)^{23}Mg(p, \gamma)^{24}Al$ effectively creating a shortcut. Since the flow rates are about equal, the effective timescale becomes the flow rate weighted harmonic mean of the two half-lives $\approx 0.10s$, which is much faster than before. This reduces the total timescale to reach ^{40}Ca to $\sim 5s$. A similar shortcut exists with $^{25}Si(p, \gamma)^{26}P(p, \gamma)^{27}S(\beta^+, \nu)$ ($T_{1/2} = 0.021s$) ^{27}P competing with $^{25}Si(\beta^+, \nu)$ ($T_{1/2} = 0.188s$) $^{25}Al(p, \gamma)^{26}Si(p, \gamma)^{27}P$ however, here the proton capture Q -value is only 141keV, so the faster path is reduced by photodisintegration.

At this time, the concentration of ^{31}Cl has peaked and is now being destroyed by photodisintegration. Therefore the flow must pass through the $^{30}S(\beta^+, \nu)$ ($T_{1/2} = 1.08s$) reaction, which is the slowest weak reaction in the flow and adds about a second to the total timescale.

Reaching ^{31}S the flow now branches again. Instead of going through the slower $^{31}S(\beta^+, \nu)$ ($T_{1/2} = 2.13s$) $^{31}P(p, \gamma)^{32}S(p, \gamma)^{33}Cl$, the flow can now go directly through either $^{31}S(p, \gamma)^{32}Cl(\beta^+, \nu)$ ($T_{1/2} = 0.293s$) $^{32}S(p, \gamma)^{33}Cl$ or $^{31}S(p, \gamma)^{32}Cl(p, \gamma)^{33}Ar(\beta^+, \nu)$ ($T_{1/2} = 0.153s$) ^{33}Cl which shaves another 2 seconds off the characteristic time for the rp -process.

The flow now breaks into the pf -shell nuclei by proton-captures on ^{39}Ca and ^{40}Ca (Wiescher & Görres (1989)). The very fast β^+ -decays on the highly radioactive Sc and Ti isotopes cause the flow to spread (Fig.6) and makes an analysis of the timescales difficult.

The hot CNO like cycle discussed in the previous section now has proton capture break-outs on via $^{42}Ti(p, \gamma)^{43}V$ and $^{43}Ti(p, \gamma)^{44}V$ and $^{43}Sc(p, \gamma)^{44}Ti$.

These reaction pass through ^{43}V and ^{44}V and after several combination of proton capture and beta decays, the flow goes through the ^{45}V bottleneck which can only happen through either a β^+ -decay ($T_{1/2} = 0.59s$) or a proton capture to ^{46}Cr . The next bottleneck is ^{48}Cr which can be reached from ^{46}V by either $^{46}V(\beta^+, \nu)$ ($T_{1/2} = 0.429s$) $^{46}Ti(p, \gamma)^{47}Ti(p, \gamma)^{48}Cr$

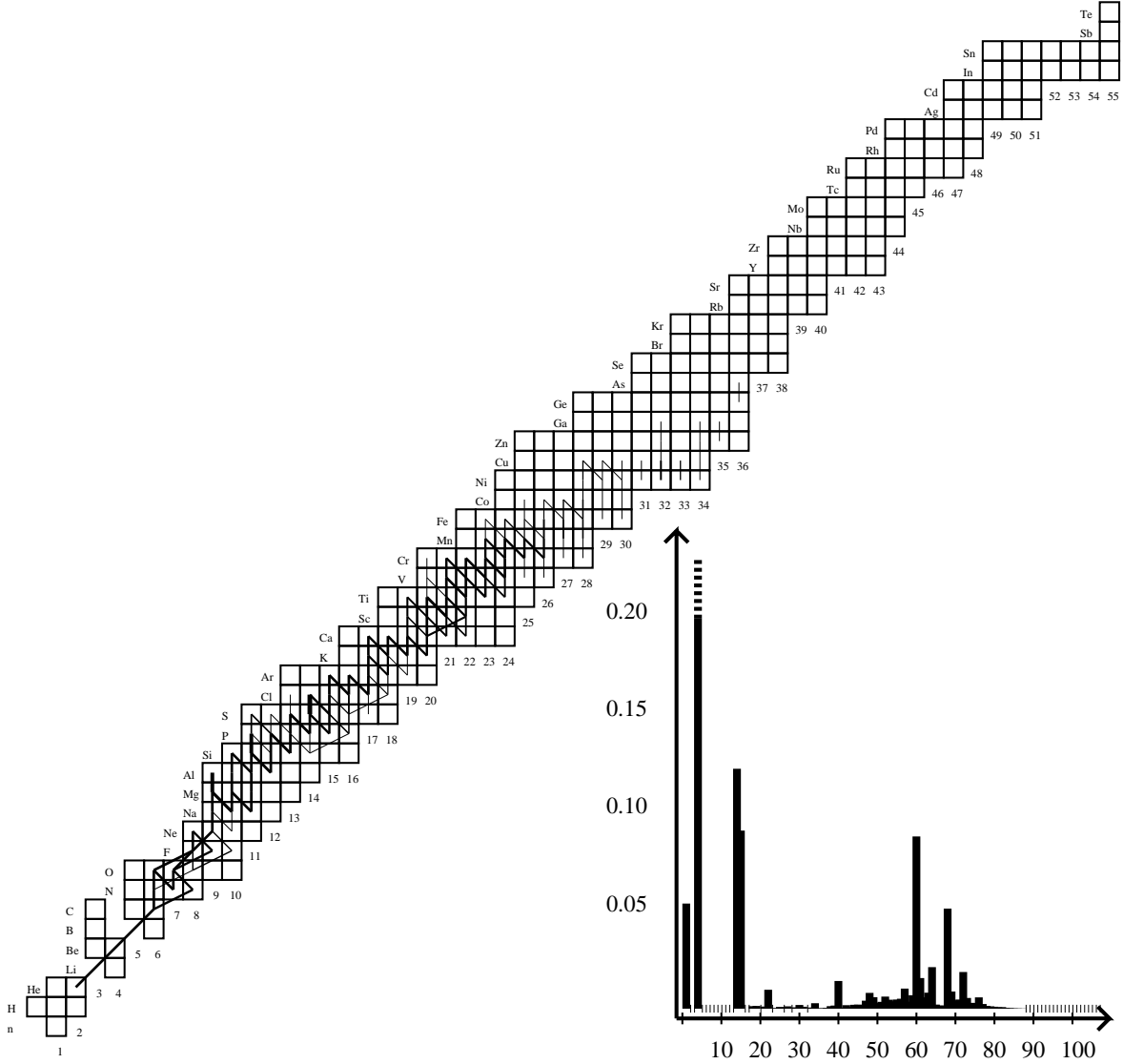


Fig. 6.— Ignition: $T = 3.99 \cdot 10^8 \text{K}$, $\rho = 6.41 \cdot 10^5 \text{g/cm}^3$, $X = 0.05$, $Y = 0.36$, $t = -12.938 \text{s}$. (see end of §4 for an explanation of the diagram).

or $^{46}\text{V}(p, \gamma) ^{47}\text{Cr}(\beta^+, \nu)$ ($T_{1/2} = 0.497\text{s}$) $^{47}\text{V}(p, \gamma) ^{48}\text{Cr}$ or $^{46}\text{V}(p, \gamma) ^{47}\text{Cr}(p, \gamma) ^{48}\text{Mn}(\beta^+, \nu)$ ($T_{1/2} = 0.030\text{s}$) ^{48}Cr .

The ^{48}Cr bottleneck has a half life of $T_{1/2} = 2.02\text{h}$ which makes it “stable” on the timescale of the burst. The $^{48}\text{Cr}(p, \gamma) ^{49}\text{Mn}$ reaction is therefore important at this stage because it is the only way for the flow to proceed.

After capturing a proton the flow proceeds from ^{49}Mn to ^{50}Mn via either a beta decay followed by a proton capture or vice versa. The flow from ^{50}Mn to ^{51}Mn proceeds in a similar manner. The ^{51}Mn isotope has a half life of $T_{1/2} = 35.3\text{m}$ so ^{51}Mn captures a proton and becomes ^{52}Fe .

There is a slight flow out of ^{52}Fe that moves to ^{56}Fe via a series of proton captures followed by beta decays. At this point ^{56}Fe captures several protons to ^{59}Cu which decays and proton captures and decays to ^{60}Ni . There are also proton captures on Ni-Zn ashes from the previous burst at this time.

4.1.3. Fig. 7: $T = 5.37 \cdot 10^8\text{K}$, $\rho = 5.81 \cdot 10^5\text{g/cm}^3$, $X = 0.03$, $Y = 0.31$, $t = -10.631\text{s}$

At this point the $^{14}\text{O}(\alpha, p) ^{17}\text{F}$ reaction is 5 times stronger than the $^{15}\text{O}(\alpha, \gamma) ^{19}\text{Ne}$ reaction. This starts the (α, p) -proces (Wallace & Woosley (1981); Schatz et al. (1998); Fisker et al. (2004)) which here runs as $^{14}\text{O}(\alpha, p) ^{17}\text{F}(p, \gamma) ^{18}\text{Ne}(\alpha, p) ^{21}\text{Na}(p, \gamma) ^{22}\text{Mg}(\alpha, p) ^{25}\text{Al}(p, \gamma) ^{26}\text{Si}$.

Another (α, p) -reaction exists on $^{21}\text{Mg}(\alpha, p) ^{24}\text{Al}$. This reaction soon overpowers the $^{22}\text{Al} \beta^+$ -decay from the $^{21}\text{Mg}(p, \gamma)(\gamma, p) ^{22}\text{Al}$ equilibrium which becomes largely irrelevant for the burst from this point.

While ^{31}Cl above ^{30}S is in $(p, \gamma)(\gamma, p)$ -equilibrium with ^{32}Ar , the main flow goes through the beta decay of ^{30}S which has a significant impact on the energy generation as it blocks the rest of the flow of the p -process.

In the Ca-Fe region, the flow moves closer to the dripline with $^{43}\text{V}(p, \gamma) ^{44}\text{Cr}(\beta^+, \nu)$ ($T_{1/2} = 0.030\text{s}$) ^{44}V and $^{47}\text{Mn}(p, \gamma) ^{48}\text{Fe}(\beta^+, \nu)$ ($T_{1/2} = 0.030\text{s}$) ^{48}Mn becoming more active.

Above Fe, the flow extends to ^{60}Zn as more proton rich nuclei start to capture protons. With ^{60}Zn 's $T_{1/2} = 4.10\text{m}$ halflife, ^{59}Cu 's $T_{1/2} = 83.1\text{s}$ halflife, and the stable ^{58}Ni , the $^{60}\text{Zn}(p, \gamma) ^{61}\text{Ga}$ reaction is the only way to move the flow forward.

In addition, proton captures on heavier isotopes from the previous burst moves towards the dripline. This compositional inertia increases the average mass and charge of the final

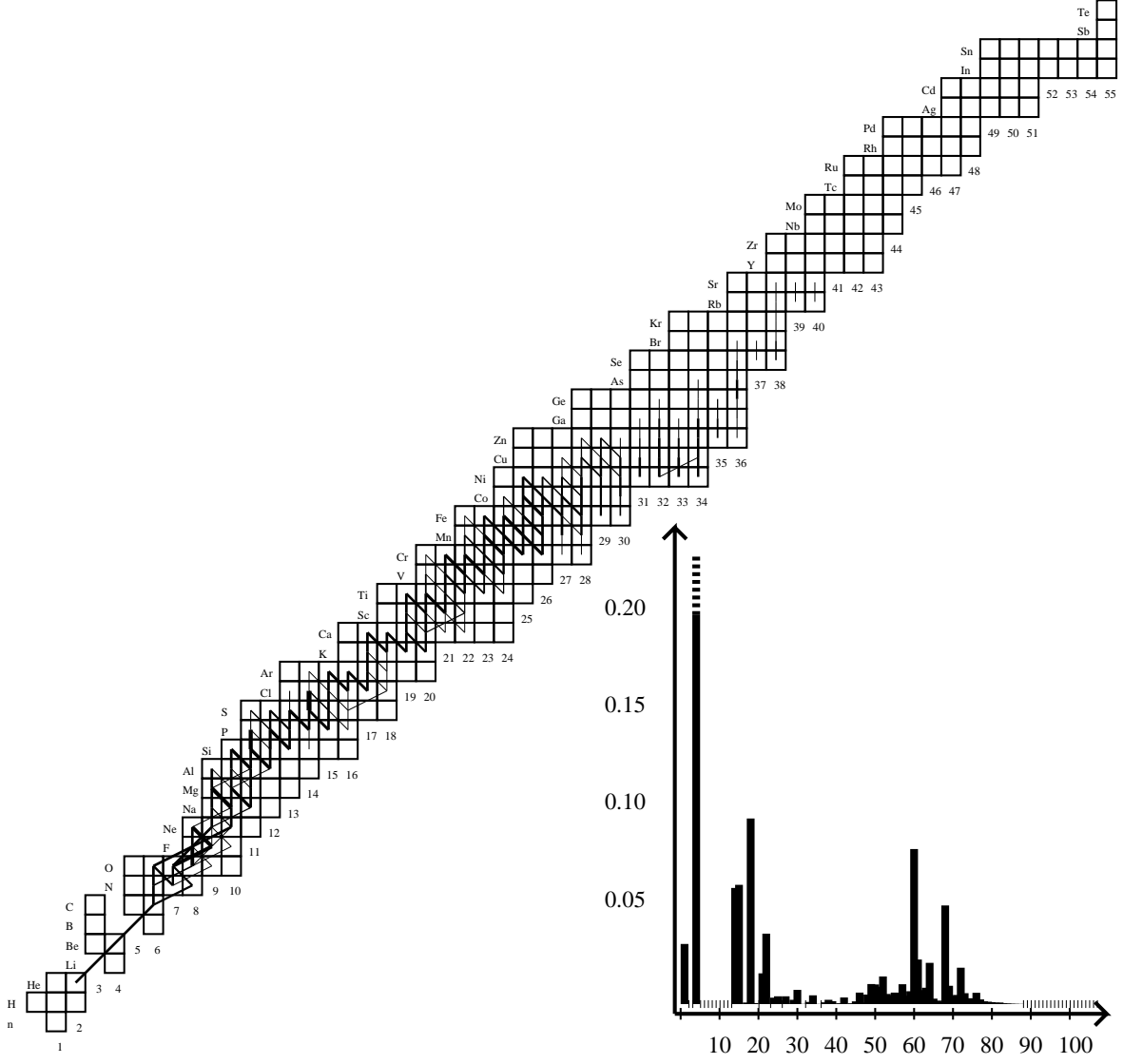


Fig. 7.— Ignition: $T = 5.37 \cdot 10^8 \text{K}$, $\rho = 5.81 \cdot 10^5 \text{g/cm}^3$, $X = 0.03$, $Y = 0.31$, $t = -10.631 \text{s}$. (see end of §4 for an explanation of the diagram).

ashes.

4.1.4. *Fig. 8:* $T = 7.30 \cdot 10^8 K$, $\rho = 5.07 \cdot 10^5 g/cm^3$, $X = 3.5 \times 10^{-4}$, $Y = 0.26$, $t = -9.980s$

The protons are now almost exhausted. This can also be seen in Fig. 4. Once this happens, the proton-rich isotopes near the driplines decay towards the valley of stability, where they undergo (α, p) -reactions. The figure shows the situation with less than 1% hydrogen so proton captures are still occurring although they are weakening. Also, hydrogen from (α, p) -reactions can still serve as a catalyst in the (α, p) -process.

The (α, p) -process extends further and now includes the $^{25}\text{Si}(\alpha, p) \ ^{28}\text{P}$ and $^{26}\text{Si}(\alpha, p) \ ^{29}\text{P}$ reactions.

SiPS, PSCI, ArKCa, and CaScTi cycles are observed with ^{28}Si , ^{32}P , ^{36}Ar and ^{40}Ca as the nexus, but they are not consequential to the flow.

In the Zn region, the flow proceeds via $^{59}\text{Cu}(\beta^+, \nu)$ ($T_{1/2} = 84.5s$) as the proton captures on ^{60}Zn remain weak. This flow reaches ^{63}Ge and ^{64}Ge but will not move further in this region as the hydrogen concentration is rapidly depleting.

4.1.5. *Fig. 9:* $T = 9.03 \cdot 10^8 K$, $\rho = 4.46 \cdot 10^5 g/cm^3$, $X = 3.3 \times 10^{-6}$, $Y = 0.12$, $t = -8.075s$

At this point the region receives more heat from adjacent regions than it produces. This allows endothermic (α, p) -reactions on better bound nuclei.

Presently, sufficient material has been moved to the ^{60}Zn isotope ensuring its decay and extending the rp -process from light isotopes into heavier isotopes. However, the only protons available for capture on these heavy nuclei come from (α, p) -reactions on $A = 20\text{--}36$ so the general lack of protons ensures that the rp -process at this point does not proceed beyond $A = 64$. Additionally the shortage of protons means that the flow moves away from the proton dripline with the remaining protons generally capturing on the currently most abundant nuclei (now determined by half-life) with the largest cross sections and the lowest Coulomb barriers, that is, $A = 20\text{--}36$.

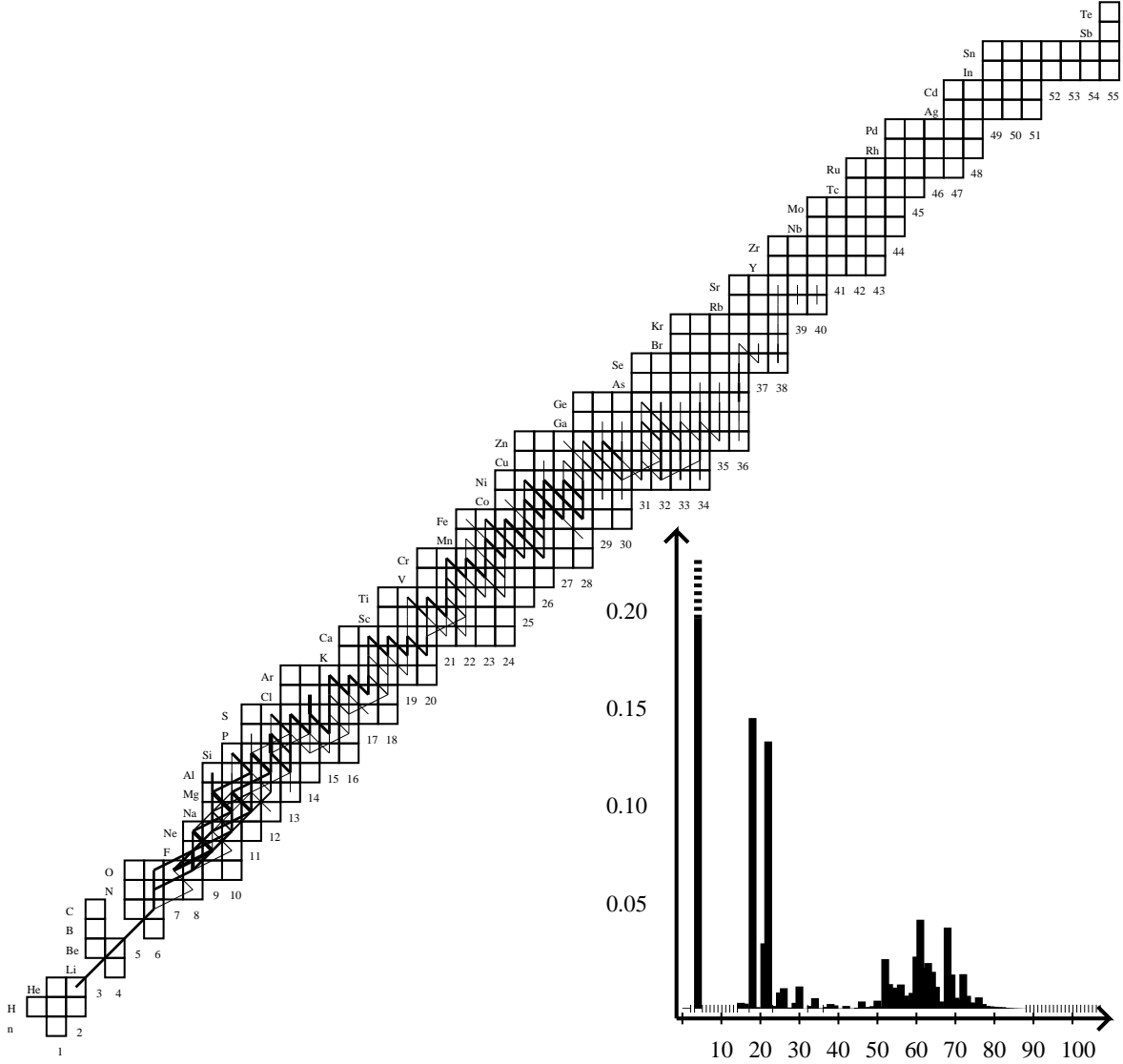


Fig. 8.— Ignition: $T = 7.30 \cdot 10^8 \text{K}$, $\rho = 5.07 \cdot 10^5 \text{g/cm}^3$, $X = 3.5 \times 10^{-4}$, $Y = 0.26$, $t = -9.980 \text{s}$. (see end of §4 for an explanation of the diagram).

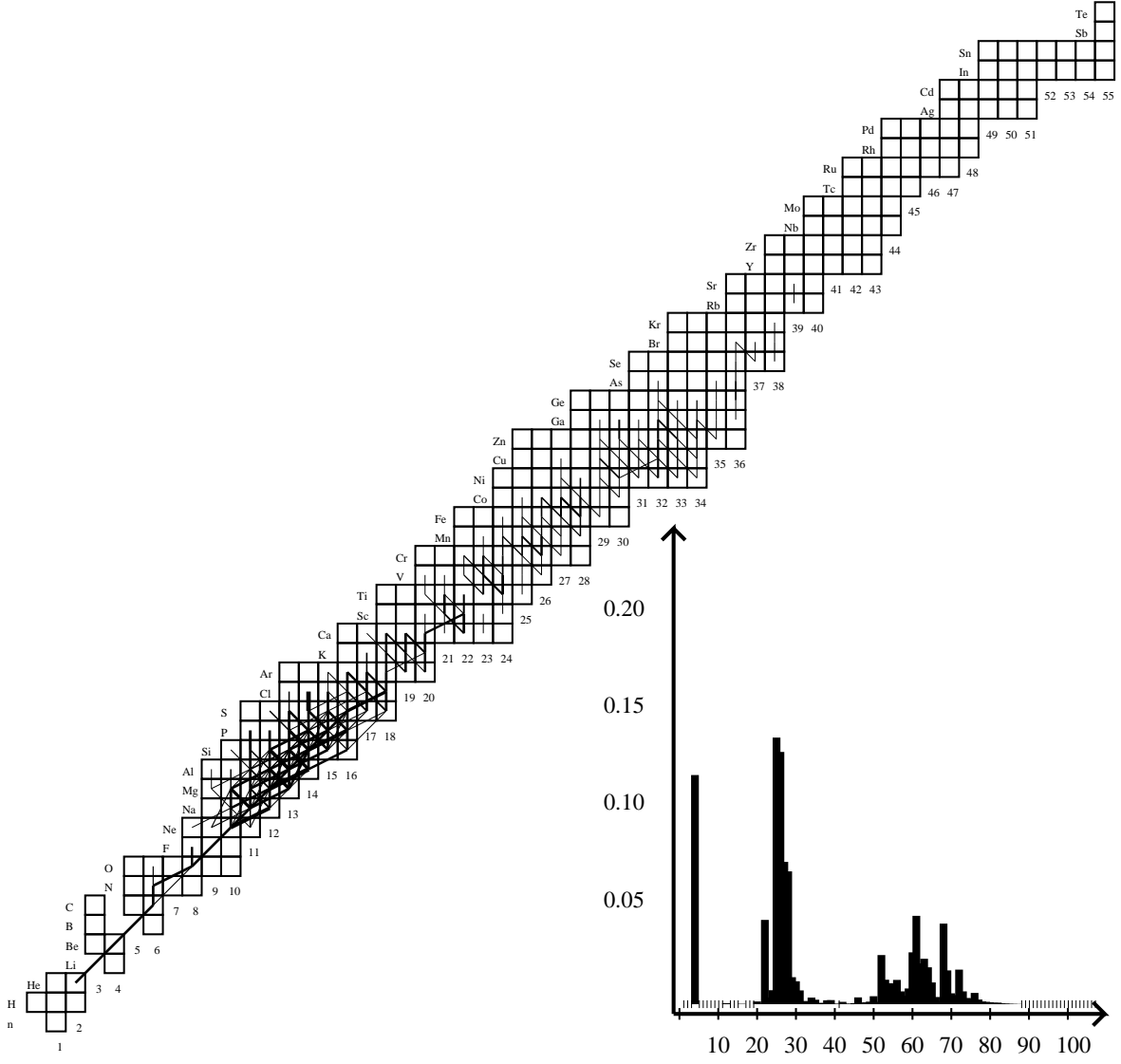


Fig. 9.— Ignition: $T = 9.03 \cdot 10^8 \text{K}$, $\rho = 4.46 \cdot 10^5 \text{g/cm}^3$, $X 3.3 \times 10^{-6}$, $Y = 0.12$, $t = -8.075 \text{s}$. (see end of §4 for an explanation of the diagram).

4.1.6. *Fig. 10:* $T = 9.89 \cdot 10^8 K$, $\rho = 4.20 \cdot 10^5 g/cm^3$, $X = 2.4 \times 10^{-9}$, $Y = 0.05$,
 $X_{28} = 0.22$, $t = -3.018s$

The flow through the alpha-chain nuclei is clearly seen in Fig. 10 which shows the reaction flow at the time where maximum temperature is achieved. Notice that $^{12}C(p, \gamma)^{13}N(\alpha, p)^{16}O$ is much stronger than the direct $^{12}C(\alpha, \gamma)^{16}O$ -reaction as long as the (α, p) -reactions are still possible on heavier isotopes (Weinberg et al. 2006).

The reaction flow continues with (α, γ) -reactions up to ^{36}Ar . Eventually the downward heat flux from the upper regions becomes too weak to sustain the (α, p) -reactions and the reactions die out leaving only radioactive isotopes, which slowly decay to stabler ones.

4.2. Above the ignition region

It is relevant to know the reaction flow and its energy release at the depth, which reach the highest temperature during the burst, because it heats up adjacent and colder regions. This is because heat is transported as electrons and photons are diffused along a negative temperature gradient. The highest temperature of a burst ignited by mixed hydrogen and helium is reached just above the point of point of ignition.

4.2.1. *Fig. 11:* $T = 2.80 \cdot 10^8 K$, $\rho = 4.29 \cdot 10^5 g/cm^3$, $X = 0.41$, $Y = 0.43$, $t = -103.078s$

The $^{15}O(\alpha, \gamma)^{19}Ne$ -reaction is less important at this depth, because less “hot CNO material” has been created due to lower operating temperatures and densities of the triple-alpha process. So while the reaction burns off the existing ^{15}O , the runaway at this depth occurs, when the heat from the ignition point below increases the 3α reaction, so the $^{12}C(p, \gamma)^{13}N(p, \gamma)^{14}O(\alpha, p)^{17}F$ reaction path dominates the eventual runaway. This is because ^{14}O ($T_{1/2} = 70.6s$) does not have the time to decay during the runaway. However, at this point the $^{15}O(\alpha, \gamma)^{19}Ne$ -reaction does establish a very weak flow to the iron-region along a flow path identical to the initial path in the deeper region.

Although this region contains former surface ashes there are no further captures beyond these isotopes at the present time.

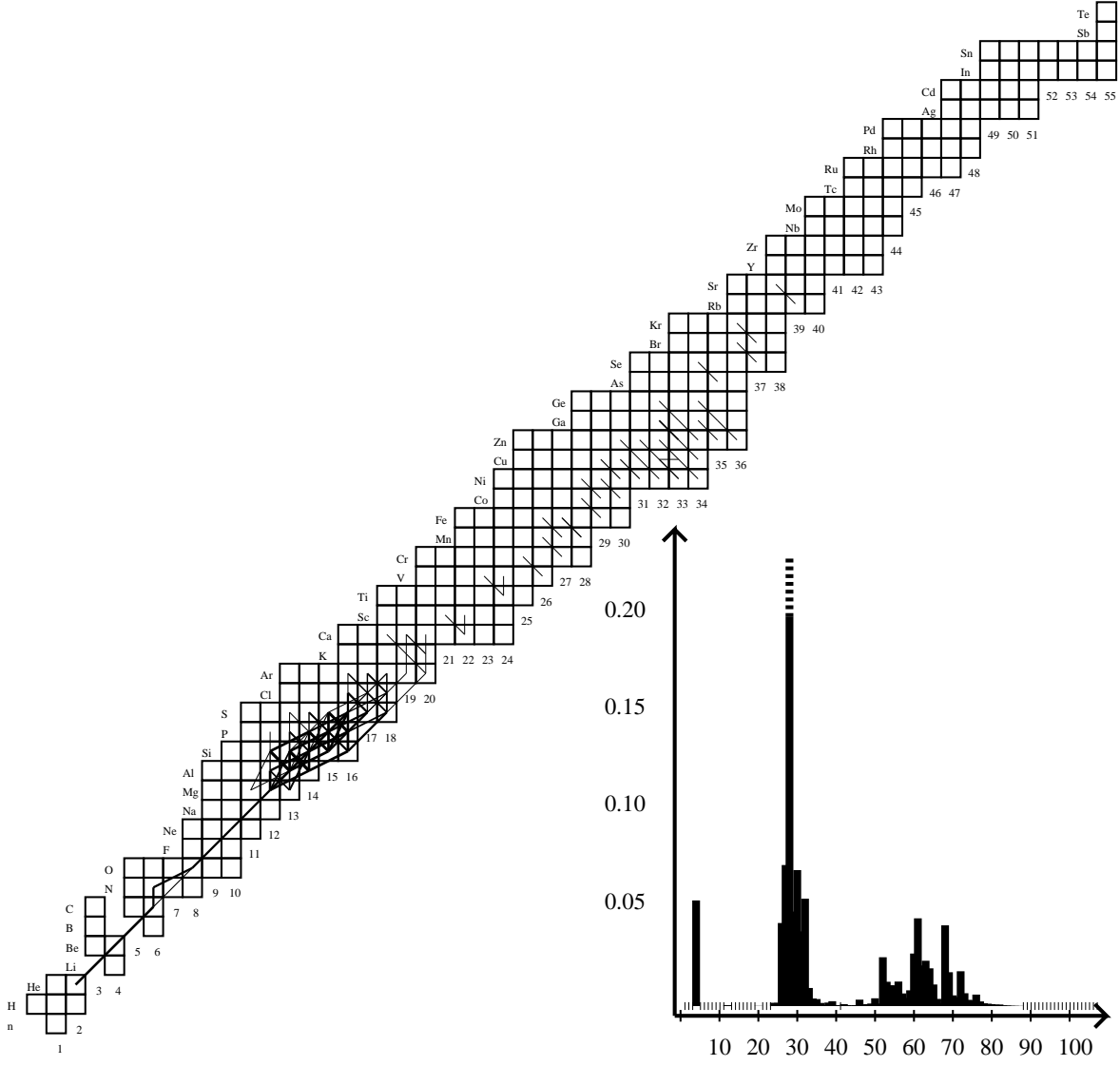


Fig. 10.— Ignition: $T = 9.89 \cdot 10^8 \text{K}$, $\rho = 4.20 \cdot 10^5 \text{g/cm}^3$, $X = 2.4 \times 10^{-9}$, $Y = 0.05$, $X_{28} = 0.22$, $t = -3.018 \text{s}$. (see end of §4 for an explanation of the diagram).

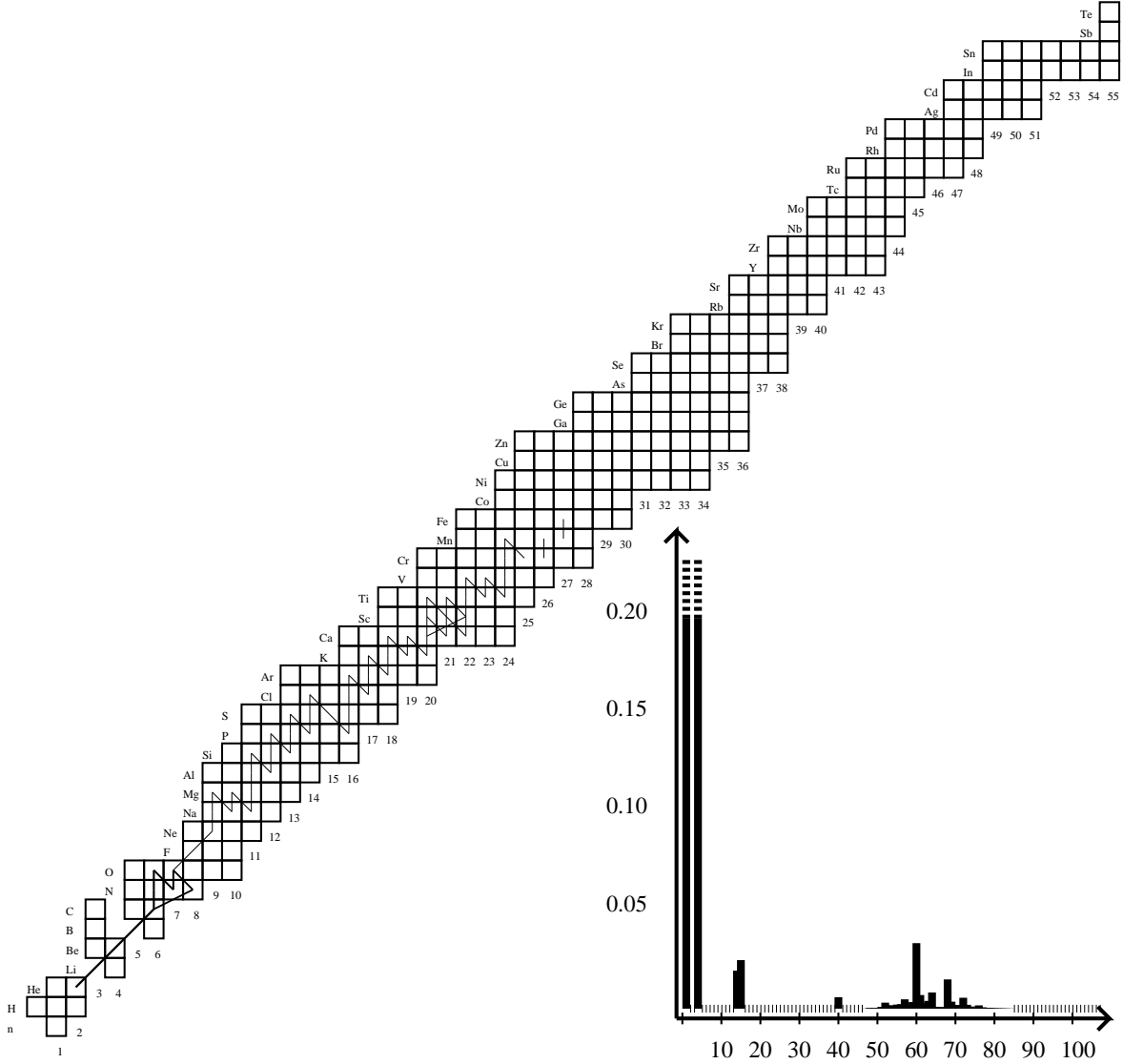


Fig. 11.— Above ignition: $T = 2.80 \cdot 10^8 \text{K}$, $\rho = 4.29 \cdot 10^5 \text{g/cm}^3$, $X = 0.41$, $Y = 0.43$, $t = -103.078 \text{s}$. (see end of §4 for an explanation of the diagram).

4.2.2. *Fig. 12:* $T = 3.97 \cdot 10^8 K$, $\rho = 3.68 \cdot 10^5 g/cm^3$, $X = 0.400$, $Y = 0.406$, $t = -12.387s$

At this point $^{14}O(\alpha, p)^{17}F$ reaction reaches 1/3 of the flow rate of the $^{15}O(\alpha, \gamma)^{19}Ne$ -reaction. This happens at a lower temperature for this depth, because the $^{14}O/^{15}O$ abundance-ratio is relatively higher.

The breakout establishes the second hot CNO bi-cycle (discussed in §4.1.2); in contrast to the ignition point, the first bi-cycle (discussed in §4.1) is not established, because it is already sufficiently hot and there is sufficient hydrogen to capture on ^{19}Ne destroying it immediately.

The heat flux building up rapidly from the ignition point below means that short cuts e.g. $^{22}Mg(p, \gamma)^{23}Al(p, \gamma)^{24}Si(\beta^+, \nu)$ ($T_{1/2} = 0.190s$) ^{24}Al competing with $^{22}Mg(\beta^+, \nu)$ ($T_{1/2} = 3.37s$) $^{22}Na(p, \gamma)^{23}Mg(p, \gamma)^{24}Al$ quickly becomes dominated by the leg closest to the proton dripline.

From this point the reactions are identical to the flow described in §4.1.2. Since there is more hydrogen in this region the reaction on isotopes heavier than Mn are faster, yet since the temperature at this point in time (same as §4.1.2) is lower, the the capture rates on lighter isotopes than Mn are slower.

4.2.3. *Fig. 13:* $T = 4.44 \cdot 10^8 K$, $\rho = 3.46 \cdot 10^5 g/cm^3$, $X = 0.398$, $Y = 0.402$, $t = -11.091s$

$^{14}O(\alpha, p)^{17}F$ is now as strong as $^{15}O(\alpha, \gamma)^{19}Ne$. The flow through the $^{31}Cl(\beta^+, \nu)$ ($T_{1/2} = 0.270s$) waiting point is currently approximately equal to the flow through the ^{30}S ($T_{1/2} = 1.08s$) waiting point, but the latter will quickly become dominant as rising temperatures prevent the formation of ^{31}Cl due photodisintegration.

In the Zn region, the flow stops at the long lived ^{59}Cu ($T_{1/2} = 84.7s$) and ^{60}Zn ($T_{1/2} = 4.29m$), but the temperature is not yet sufficiently high for proton captures to established a reaction flow to heavier nuclei, nor has sufficient time passed to allow a substantial amount of material to decay through these two nuclei. It is interesting to note that processing to heavier material either depends on the temperature becoming sufficiently high for the $^{60}Zn(p, \gamma)(\gamma, p)^{61}Ga$ equilibrium to allow (p, γ) -reactions on ^{61}Ga or the temperature remaining sufficiently low for the flow to decay through the faster $^{59}Cu(\beta^+, \nu)^{59}Ni$ -reaction.

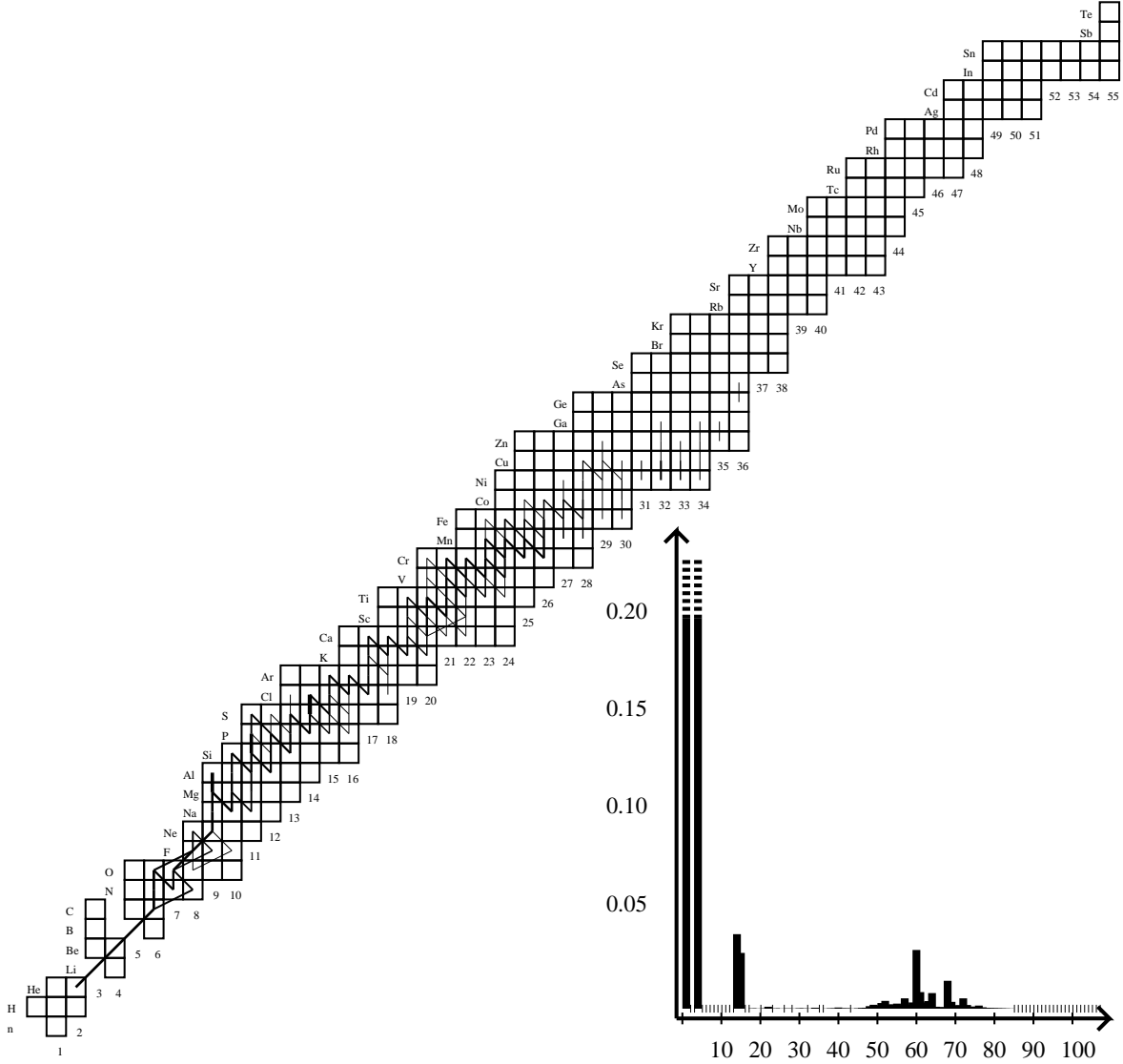


Fig. 12.— Above ignition: $T = 3.97 \cdot 10^8 \text{K}$, $\rho = 3.68 \cdot 10^5 \text{g/cm}^3$, $X = 0.400$, $Y = 0.406$, $t = -12.387 \text{s}$. (see end of §4 for an explanation of the diagram).

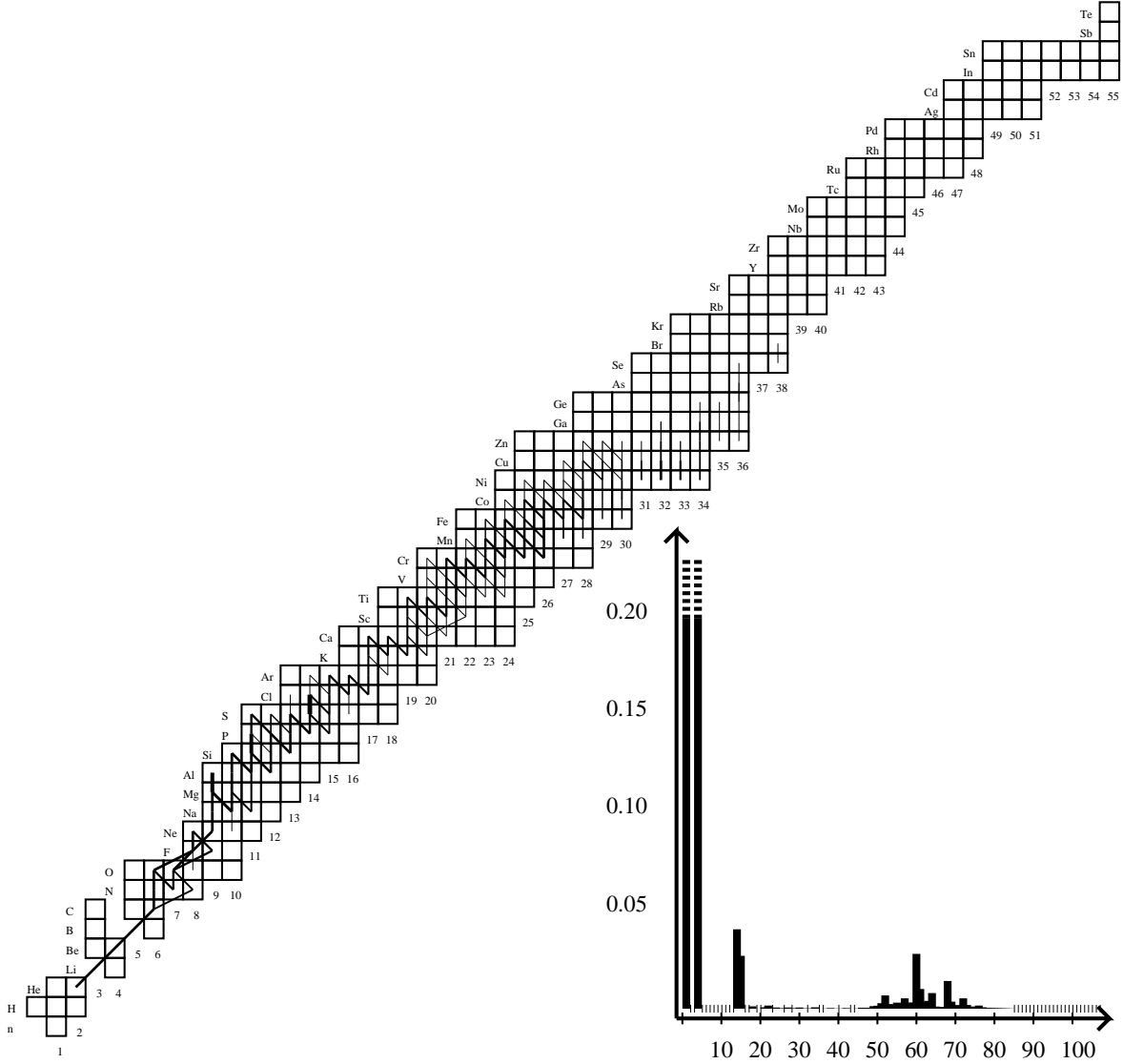


Fig. 13.— Above ignition: $T = 4.44 \cdot 10^8 \text{K}$, $\rho = 3.46 \cdot 10^5 \text{g/cm}^3$, $X = 0.398$, $Y = 0.402$, $t = -11.091 \text{s}$. (see end of §4 for an explanation of the diagram).

4.2.4. *Fig. 14:* $T = 5.75 \cdot 10^8 K$, $\rho = 2.19 \cdot 10^5 g/cm^3$, $X = 0.393$, $Y = 0.387$, $t = -10.418s$

At this point the $^{18}\text{Ne}(\alpha, p)^{21}\text{Na}$ -reaction activates making it possible to move into the rp -process via $^{12}\text{C}(p, \gamma)^{13}\text{N}(p, \gamma)^{14}\text{O}(\alpha, p)^{17}\text{F}(p, \gamma)^{18}\text{Ne}(\alpha, p)^{21}\text{Na}$ and so forth instead of waiting for the $T_{1/2} = 1.67s$ beta-decay of ^{18}Ne . The $^{18}\text{Ne}(\alpha, p)^{21}\text{Na}$ -reaction is thus especially important as most of the energy release in the atmosphere originate in the rp -process at lower depths/higher hydrogen concentrations as seen in Fig. 2.

However, presently 90% of the the flow through the lighter isotopes stops at the ^{30}S ($T_{1/2} = 1.09s$) waiting point with only a small flux following from its decay. This causes a temporary dip in the energy production, though the higher temperature ensures a flow close to the dripline from Ca to Ni. This flow is, however, slowed down at the $N = 28$ isotones due to the long half-lives of ^{55}Co ($T_{1/2} = 10.3h$) and ^{56}Ni ($T_{1/2} = 24.9h$) which effectively prevents any beta decays of these isotopes. It is also interesting to note the (p, α) -reactions on the heavier Cu isotopes going back to Ni while releasing hydrogen.

At this point there is a weak flow out of ^{59}Cu which allows additional proton captures viz. $^{59}\text{Ni}(p, \gamma)^{60}\text{Cu}(p, \gamma)^{61}\text{Zn}(p, \gamma)^{62}\text{Ga}$ which can either decay or capture an additional proton to ^{63}Ge which then decays. If ^{62}Ga decays it captures two additional protons and goes to ^{64}Ge . It is also possible to reach ^{65}Ge if ^{63}Ga decays.

Heavier isotopes are generated through proton captures on ashes from the previous burst. None of these are beta decaying though.

4.2.5. *Fig. 15:* $T = 6.97 \cdot 10^8 K$, $\rho = 2.51 \cdot 10^5 g/cm^3$, $X = 0.381$, $Y = 0.372$, $t = -9.994s$

A couple of seconds after its breakout, $^{14}\text{O}(\alpha, p)^{17}\text{F}$, becomes so fast that any ^{14}O is immediately destroyed. Consequently ^{15}O is only created via the hot CNO bi-cycle. However, the bi-cycle will become void, because it is now sufficiently hot for alpha-particles to penetrate the Coulomb barrier of ^{18}Ne , thus skipping its $T_{1/2} = 1.67s$ β^+ -decay.

Additional (α, p) -captures now happen on ^{21}Mg and ^{25}Si . The latter circumvents the ($T_{1/2} = 0.176s$) half-life of ^{25}Si , thus shortening the characteristic reaction flow timescale in the $A = 20$ – 30 region. The timescale is dominated by the $^{30}\text{S}(\beta^+, \nu)$ ($T_{1/2} = 1.09s$) ^{30}P reaction since 98% of the flow passes through this reaction.

Another reaction is $^{24}\text{Si}(\alpha, p)^{27}\text{P}$ but that is not as significant since ^{24}Si gets destroyed by photodisintegration. It is interesting to note a weak but present $^{18}\text{Ne}(\alpha, \gamma)^{22}\text{Mg}$ which competes with the (α, p) -process.

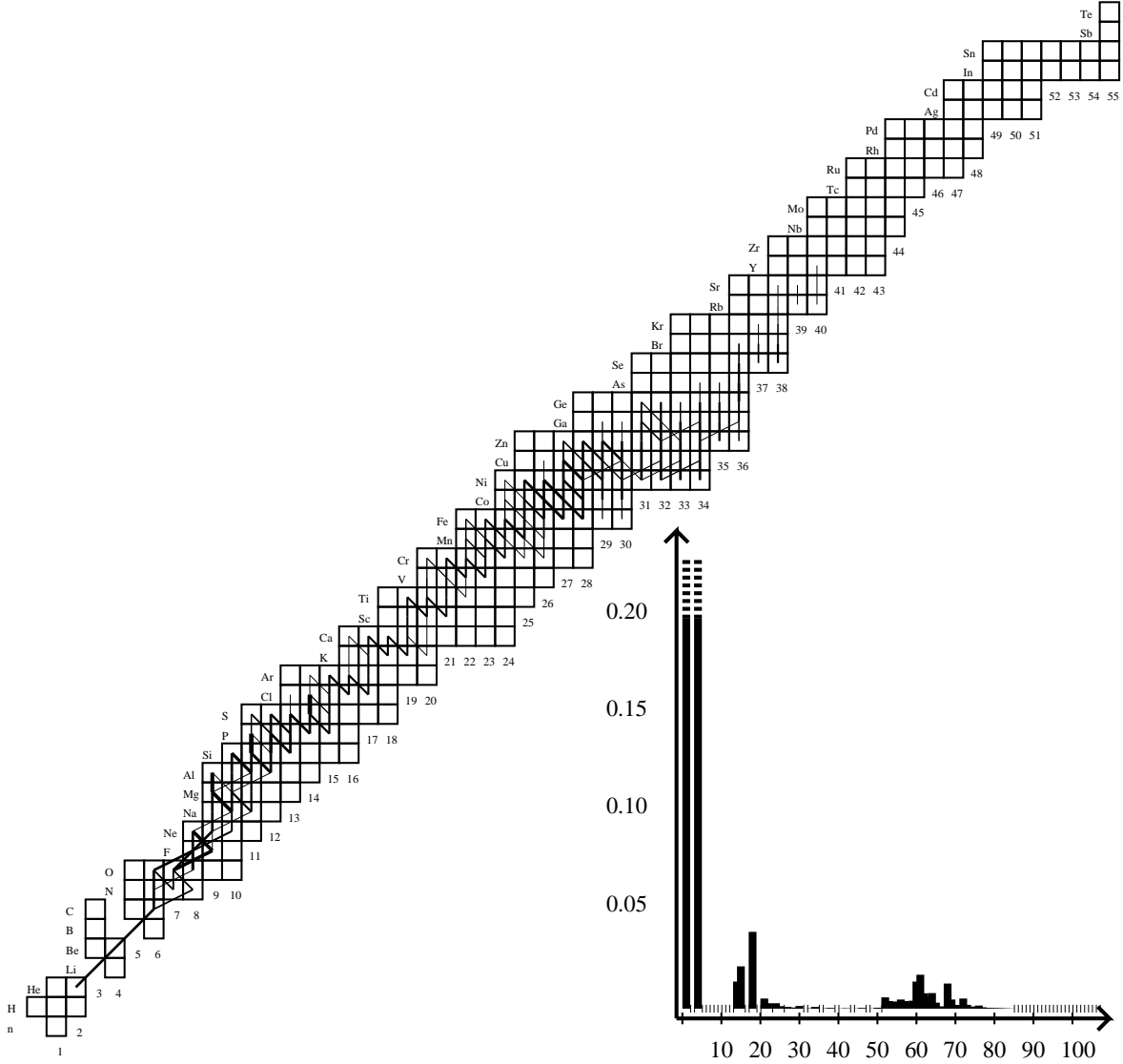


Fig. 14.— Above ignition: $T = 5.75 \cdot 10^8 \text{K}$, $\rho = 2.19 \cdot 10^5 \text{g/cm}^3$, $X = 0.393$, $Y = 0.387$, $t = -10.418 \text{s}$. (see end of §4 for an explanation of the diagram).

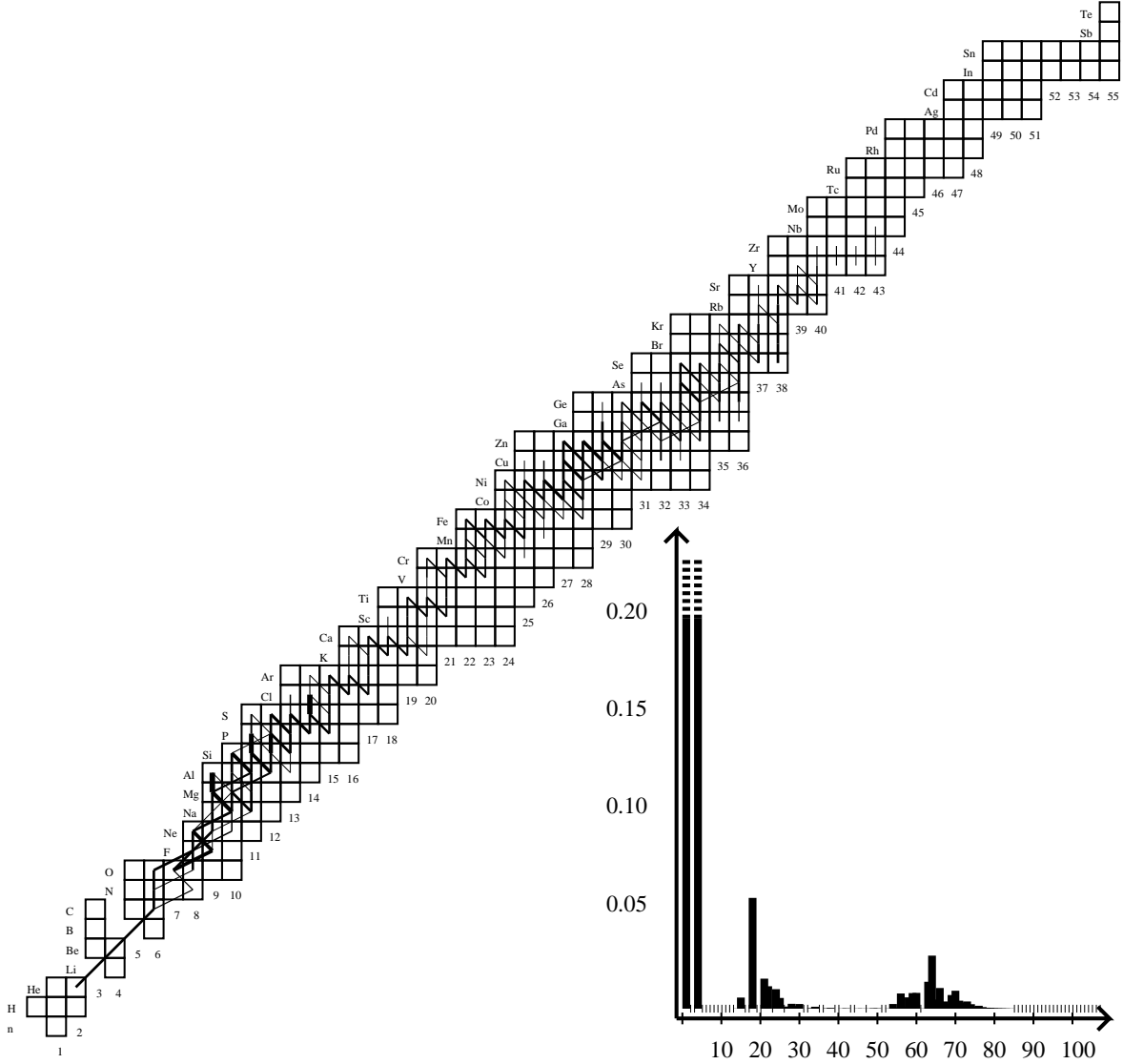


Fig. 15.— Above ignition: $T = 6.97 \cdot 10^8 \text{K}$, $\rho = 2.51 \cdot 10^5 \text{g/cm}^3$, $X = 0.381$, $Y = 0.372$, $t = -9.994 \text{s}$. (see end of §4 for an explanation of the diagram).

The flow up to ^{58}Ni remains the same. The increased temperature and flow sets up NiCuZn, ZnGaGe and GeAsSe cycles on ^{58}Ni , ^{60}Zn , and ^{66}Ge .

We note that there is still no flow out of $^{64}\text{Ge}(p, \gamma) ^{65}\text{As}$ as ^{65}As is weakly proton bound and 2p capture (Schatz et al. 1998) is not effective. Therefore the reaction flow proceeds via the slow beta decay $^{64}\text{Ge}(\beta^+, \nu)$ ($T_{1/2} = 84.9\text{s}$) ^{64}Ga or the lighter $^{63}\text{Ga}(\beta^+, \nu)$ ($T_{1/2} = 26.6\text{s}$) ^{63}Zn .

Reaching the $N = 33$ isotones, the flow reaches ^{67}Se ($T_{1/2} = 0.060\text{s}$) and ^{68}Se ($T_{1/2} = 35.5\text{s}$). Further progress either depends on another 2p-reaction (Schatz et al. 1998) or ^{68}Se or ^{67}As decaying.

As similar challenge is posed by ^{72}Kr ($T_{1/2} = 17.2\text{s}$), ^{76}Sr ($T_{1/2} = 8.9\text{s}$) and ^{80}Zr ($T_{1/2} = 3.9\text{s}$). Presently the flow has not moved farther although protons have started captures on heavier isotopes of the ashes of the previous burst.

4.2.6. Fig. 16: $T = 8.34 \cdot 10^8\text{K}$, $\rho = 2.15 \cdot 10^5\text{g/cm}^3$, $X = 0.358$, $Y = 0.346$, $t = -9.097\text{s}$

At this time the temperature is sufficiently high for photodisintegration of ^{27}S to prevent the shortcut, which was previously established between ^{25}Si and ^{27}P .

However, at the same temperature the $^{21}\text{Mg}(\alpha, p) ^{24}\text{Al}$ and the $^{22}\text{Mg}(\alpha, p) ^{25}\text{Al}$ reactions become significant. In addition, $^{24}\text{Si}(\alpha, p) ^{27}\text{P}$, $^{25}\text{Si}(\alpha, p) ^{28}\text{P}$, and $^{26}\text{Si}(\alpha, p) ^{29}\text{P}$ become significant. Circumventing the $^{30}\text{S}(\beta^+, \nu)$ ($T_{1/2} = 1.09\text{s}$) ^{30}P becomes possible through the $^{29}\text{S}(\alpha, p) ^{32}\text{Cl}$ -reaction which at this point is not as strong as the beta decay.

^{38}Ca starts photodisintegration, but since ^{39}Sc is proton unbound, the flow must await a ($T_{1/2} = 0.04\text{s}$)-decay, since this reaction is a bottleneck.

Heavier isotopes with $N > 32$ continue to ^{84}Mo ($T_{1/2} = 3.6\text{s}$). Some hydrogen is capturing on $N = 43$ and $N = 44$ isotones of the ashes from the previous burst.

4.2.7. Fig. 17: $T = 8.96 \cdot 10^8\text{K}$, $\rho = 2.07 \cdot 10^5\text{g/cm}^3$, $X = 0.327$, $Y = 0.326$, $t = -8.075\text{s}$

At this time, the $^{28}\text{S}(\alpha, p) ^{31}\text{Cl}$, $^{29}\text{S}(\alpha, p) ^{32}\text{Cl}$, and $^{30}\text{S}(\alpha, p) ^{33}\text{Cl}$ are all active. The latter now competes directly with the ^{30}S beta decay. This competition is especially important at lower accretion rates (Fisker et al. 2004).

Heavier isotopes continue to ^{88}Ru ($T_{1/2} = 1.1\text{s}$). There are no significant captures on heavier isotopes.

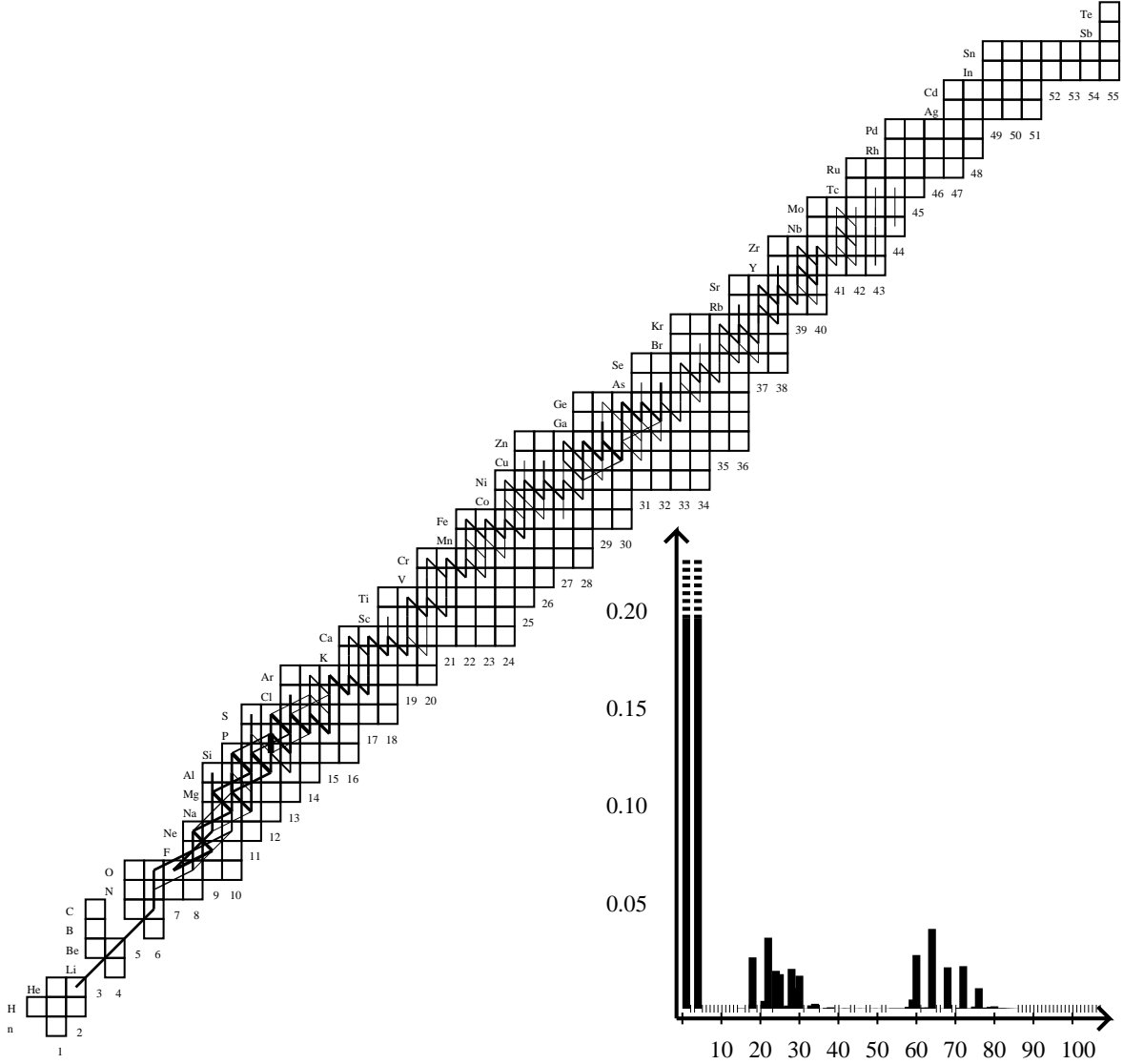


Fig. 16.— Above ignition: $T = 8.34 \cdot 10^8 \text{K}$, $\rho = 2.15 \cdot 10^5 \text{g/cm}^3$, $X = 0.358$, $Y = 0.346$, $t = -9.097 \text{s}$. (see end of §4 for an explanation of the diagram).

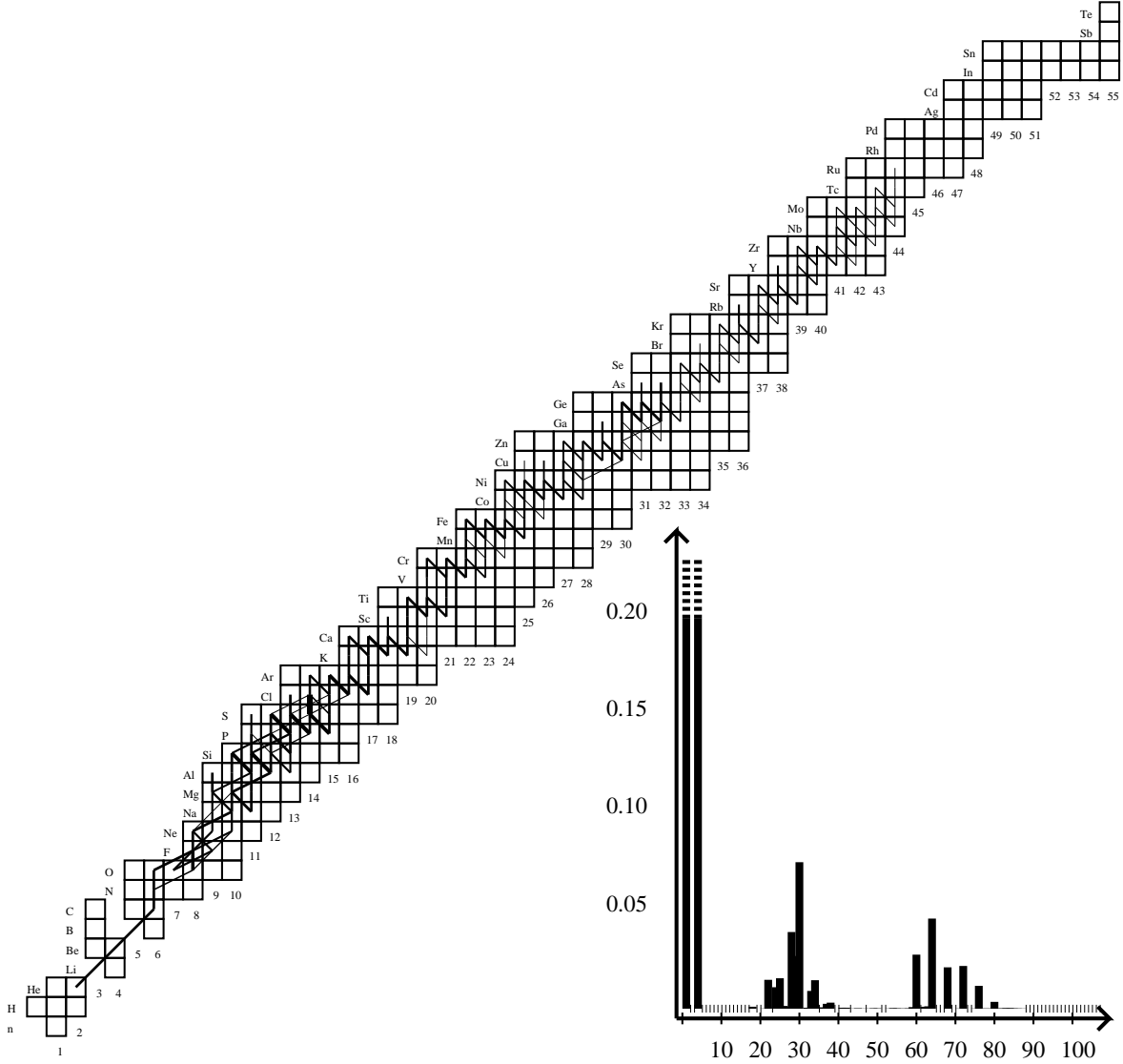


Fig. 17.— Above ignition: $T = 8.96 \cdot 10^8 \text{K}$, $\rho = 2.07 \cdot 10^5 \text{g/cm}^3$, $X = 0.327$, $Y = 0.326$, $t = -8.075 \text{s}$. (see end of §4 for an explanation of the diagram).

4.2.8. *Fig. 18:* $T = 9.93 \cdot 10^8 K$, $\rho = 2.43 \cdot 10^5 g/cm^3$, $X = 0.143$, $Y = 0.234$, $t = -3.013s$

This region has now reached its maximum temperature. The reaction flow-path is very similar to the flow in Fig. 17.

One notable difference is the $^{34}Ar(\alpha, p) ^{37}K$ reaction which is the last among the (α, p) -reactions for the temperatures encountered in type I XRBs.

Additionally, heavier isotopes continue to ^{92}Pd and ^{93}Pd . This effectively constitutes the end of the rp -process which is short of the prediction of Schatz et al. (2001a). The reason is the thermal and compositional inertia as well as the much lower peak temperature achieved by our model. If these are ignored, the flow does reach the SnSbTe cycle as shown by Woosley et al. (2004).

This flow structure is maintained until hydrogen runs out.

4.2.9. *Fig. 19:* $T = 9.62 \cdot 10^8 K$, $\rho = 3.54 \cdot 10^5 g/cm^3$, $X = 2.5 \times 10^{-5}$, $Y = 0.175$,
 $X_{60} = 0.346$, $t = 1.476s$

The last protons capture on the currently most abundant nuclei, namely the isotopes in the Ca-Ge region as the flow falls back towards the valley of stability as it is decaying along constant mass numbers.

With helium still burning, the (α, p) -process is still active along with previously mentioned (α, p) reaction up to $A = 36$. However, the $^{12}C(p, \gamma) ^{13}N(\alpha, p) ^{16}O$ path prevents much formation of ^{17}F . This means that the (α, p) -process starts on ^{21}Na which is reached from $^{16}O(\alpha, \gamma) ^{20}Ne(p, \gamma) ^{21}Na$.

4.2.10. *Fig. 20:* $T = 6.97 \cdot 10^8 K$, $\rho = 5.10 \cdot 10^5 g/cm^3$, $X = 1.0 \times 10^{-11}$, $Y = 0.089$,
 $X_{60} = 0.347$, $t = 28.788s$

Half a minute after the burst the rp -process no longer operating and the temperature has decreased 30% from the maximum temperature.

An (α, γ) -chain connects ^{16}O to ^{32}S which eliminates most of the ^{12}C via $^{12}C(p, \gamma) ^{13}N(\alpha, p) ^{16}O$. Meanwhile, heavier isotopes follow constant A decay-chains back to the valley of stability.

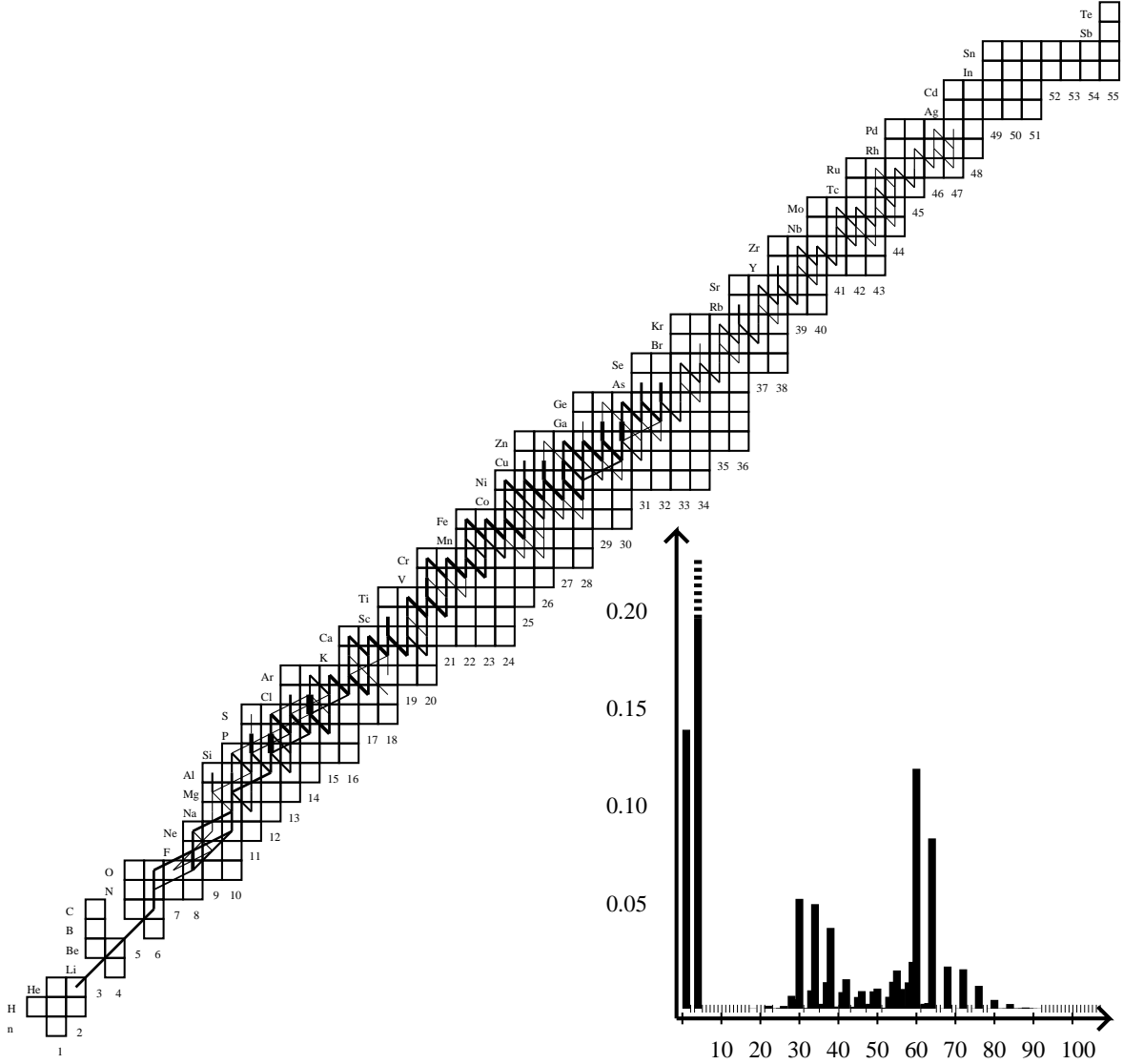


Fig. 18.— Above ignition: $T = 9.93 \cdot 10^8 \text{K}$, $\rho = 2.43 \cdot 10^5 \text{g/cm}^3$, $X = 0.143$, $Y = 0.234$, $t = -3.013 \text{s}$. (see end of §4 for an explanation of the diagram).

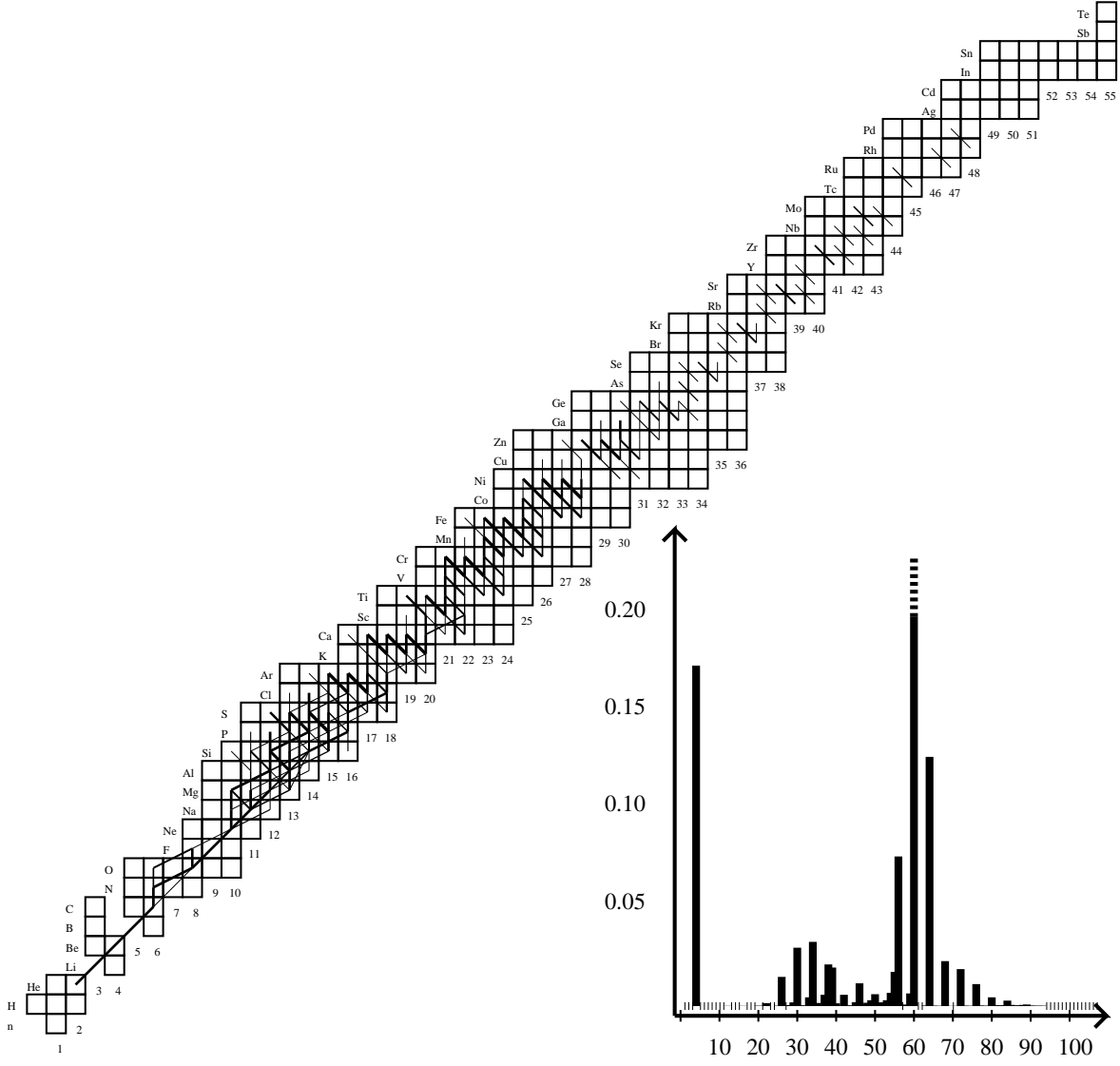


Fig. 19.— Above ignition: $T = 9.62 \cdot 10^8 \text{K}$, $\rho = 3.54 \cdot 10^5 \text{g/cm}^3$, $X = 2.5 \times 10^{-5}$, $Y = 0.175$, $X_{60} = 0.346$, $t = 1.476 \text{s}$. (see end of §4 for an explanation of the diagram).

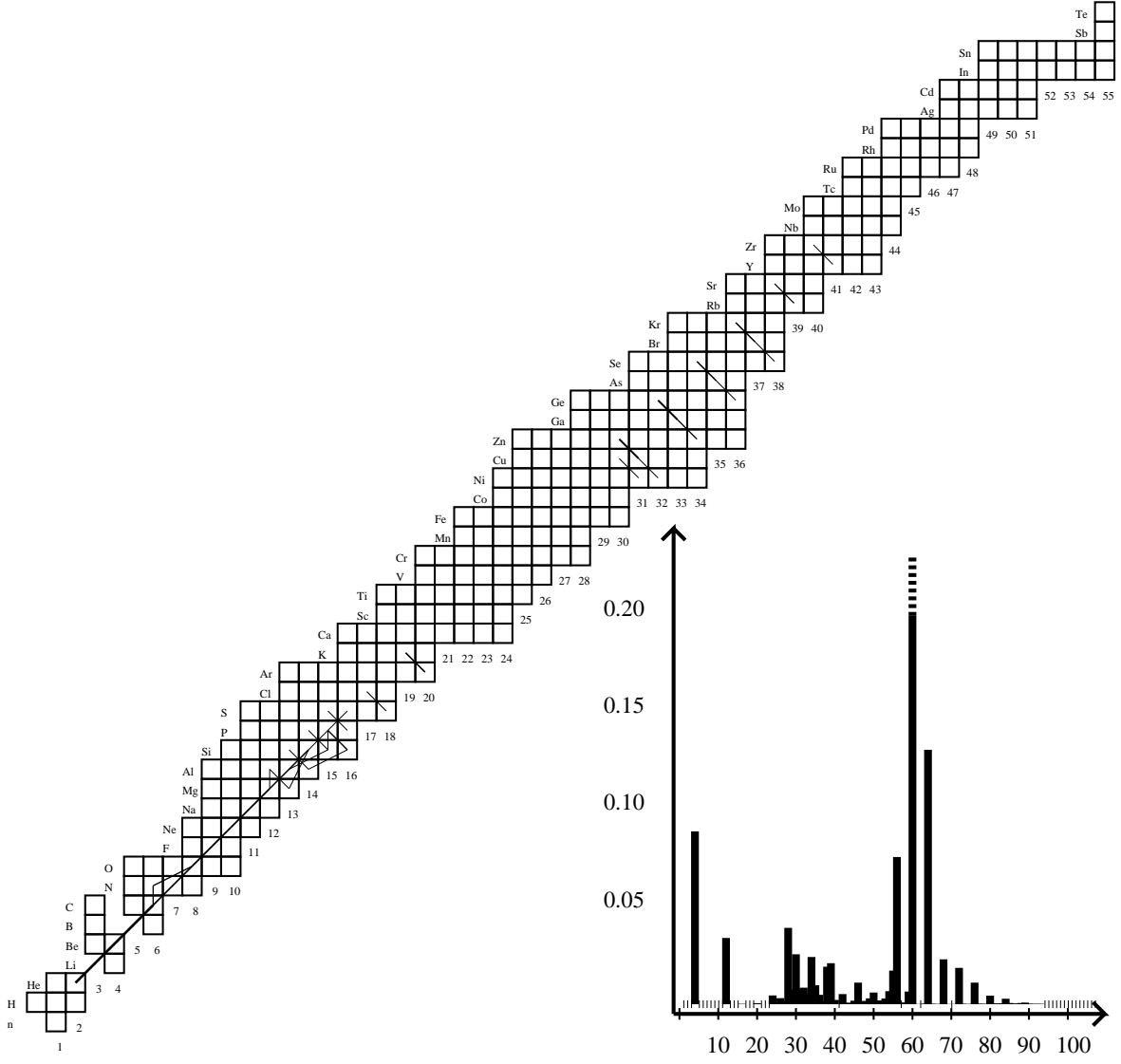


Fig. 20.— Above ignition: $T = 6.97 \cdot 10^8 \text{K}$, $\rho = 5.10 \cdot 10^5 \text{g/cm}^3$, $X = 1.0 \times 10^{-11}$, $Y = 0.089$, $X_{60} = 0.347$, $t = 28.788 \text{s}$. (see end of §4 for an explanation of the diagram).

4.3. Convective region

The size of the convective region is shown in Fig. 3, which shows a trace of the burst conditions for different depths (pressures) during a complete revolution of the limit cycle. Note that the convective zone only exist during the phase where the temperature rises (the cycle revolves clockwise). The figure shows that the convective zone does not reach the top of our model for this burst, but stays in a narrow region between $y = 5.7 \times 10^6 \text{g/cm}^2$ and $y = 5.2 \times 10^7 \text{g/cm}^2$. Additionally, this burst does not reach super-Eddington luminosities, so no ashes will be ejected by a radiatively driven wind; something which is possible in helium-ignited bursts (Weinberg et al. 2006).

The quantitative analysis of the turbulent convective burning is complicated by the mixing of matter between convective zones, which occurs as soon as and as long as a slightly superadiabatic temperature gradient is established. However, the convective timescale, $\tau_{con.} \equiv \Lambda/v_{edd.} \sim 10^{-6}\text{--}10^{-5}\text{s} \ll \tau_{rp}$, is generally faster than the typical timescale of the rp -process, so the explosive burning will have almost the same composition throughout the entire convective zone (see the convective model of Rembges (1999) which assumes identical composition throughout the convective zone for comparison) although burning happens at different temperatures and densities at the top and bottom of the convective zone respectively. Furthermore, turbulent convective burning does not happen above temperatures of $7 \times 10^8 \text{K}$, so the (α, p) -process, which has a much shorter timescale, does not become active. Therefore this region could be computed by models with a simplified description of the compositional evolution but a more complex (2D) hydrodynamical implementation. The following analysis of this region concentrates on the bottom of the convective region, because it is hotter and denser, and therefore the reactions proceed faster here.

4.3.1. Fig. 21: $T = 3.92 \cdot 10^8 \text{K}$, $\rho = 1.161 \cdot 10^4 \text{g/cm}^3$, $X = 0.610$, $Y = 0.363$, $t = -10.229 \text{s}$

The convective period during this burst lasts about 2.2s during which fresh unburned matter from the colder top of the convective zone mixes into the warmer bottom and back again. This means that temperature dependent particle-captures are effectively weaker, whereas the weak decays remain unaltered.

Due to the short duration, the region attains a maximum temperature of $\sim 0.7 \cdot 10^9 \text{K}$ while it is convecting ($\sim 0.9 \cdot 10^9 \text{K}$ at the peak), so the high temperature short cuts like (α, p) -reactions or the upper leg of rp -process bifurcations available to the deeper layers and described in the previous sections never come into play; instead the initial reaction flow is mostly represented by the flow chart of Fig. 21.

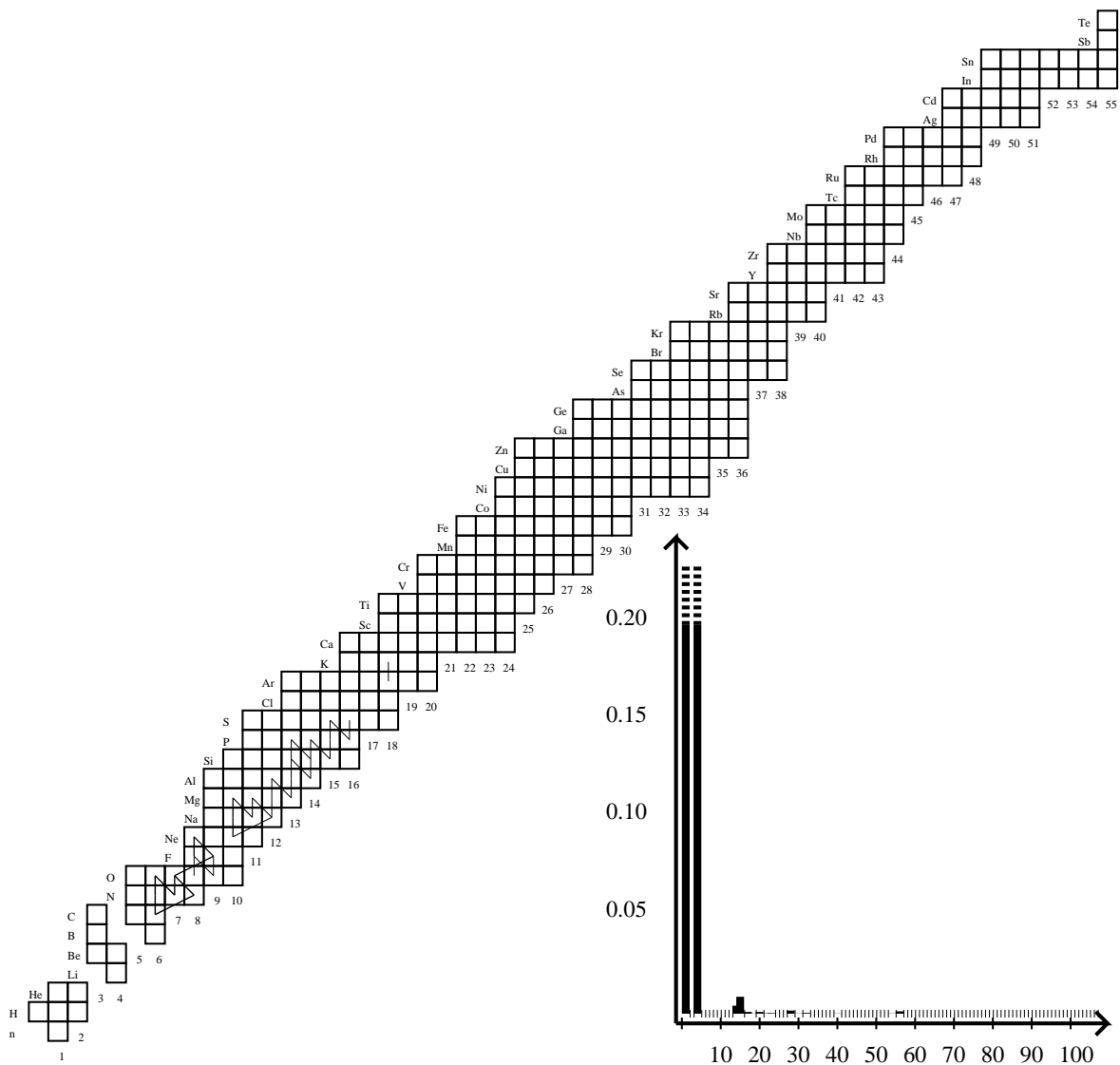


Fig. 21.— Convection region: $T = 3.92 \cdot 10^8 \text{K}$, $\rho = 1.161 \cdot 10^4 \text{g/cm}^3$, $X = 0.610$, $Y = 0.363$, $t = -10.229 \text{s}$. (see end of §4 for an explanation of the diagram).

At this point, the second hot CNO bi-cycle, $^{14}\text{O}(\alpha, p) ^{17}\text{F}(p, \gamma) ^{18}\text{Ne}(\beta^+, \nu)$ ($T_{1/2} = 1.67\text{s}$) $^{18}\text{F}(p, \alpha) ^{15}\text{O}$ already dominates the first hot CNO bi-cycle, $^{19}\text{Ne}(\beta^+, \nu)$ ($T_{1/2} = 17.2\text{s}$) $^{19}\text{F}(p, \alpha) ^{16}\text{O}(p, \gamma) ^{17}\text{F}(p, \gamma) ^{18}\text{Ne}(\beta^+, \nu)$ ($T_{1/2} = 1.67\text{s}$) $^{18}\text{F}(p, \alpha) ^{15}\text{O}$, as the temperature is high enough for the $^{19}\text{Ne}(p, \gamma) ^{20}\text{Na}$ -reaction to dominate the slow $^{19}\text{Ne}(\beta^+, \nu)$ ($T_{1/2} = 17.2\text{s}$) ^{19}F . From this point ^{20}Na captures another proton so $^{20}\text{Na}(p, \gamma) ^{21}\text{Mg}(\beta^+, \nu)$ ($T_{1/2} = 0.124\text{s}$) $^{21}\text{Na}(p, \gamma) ^{22}\text{Mg}$.

Here the flow bifurcates to either $^{22}\text{Mg}(\beta^+, \nu)$ ($T_{1/2} = 3.46\text{s}$) $^{22}\text{Na}(p, \gamma) ^{23}\text{Mg}(p, \gamma) ^{24}\text{Al}$ or $^{22}\text{Mg}(p, \gamma) ^{23}\text{Al}(p, \gamma) ^{24}\text{Si}(\beta^+, \nu)$ ($T_{1/2} = 0.191\text{s}$) ^{24}Al . A similar bifurcation exists at $^{25}\text{Si}(p, \gamma) ^{26}\text{P}(p, \gamma) ^{27}\text{S}(\beta^+, \nu)$ ($T_{1/2} = 0.021\text{s}$) ^{27}P competing with $^{25}\text{Si}(\beta^+, \nu)$ ($T_{1/2} = 0.189\text{s}$) $^{25}\text{Al}(p, \gamma) ^{26}\text{Si}(p, \gamma) ^{27}\text{P}$.

The ^{30}S waiting point still acts as a bottleneck with a small leak via $^{30}\text{S}(p, \gamma) ^{31}\text{Cl}(\beta^+, \nu)$ ($T_{1/2} = 0.272\text{s}$) ^{30}S . However, this is quickly reduced by photodisintegration as before.

This flow passes through the $^{34}\text{Ar}(\beta^+, \nu)$ ($T_{1/2} = 0.824\text{s}$) bottleneck and on through $^{37}\text{Ca}(\beta^+, \nu)$ ($T_{1/2} = 0.155\text{s}$) $^{37}\text{K}(p, \gamma) ^{38}\text{Ca}(\beta^+, \nu)$ ($T_{1/2} = 0.423\text{s}$) $^{38}\text{K}(p, \gamma) ^{39}\text{Ca}(\beta^+, \nu)$ ($T_{1/2} = 0.808\text{s}$) $^{39}\text{K}(p, \gamma) ^{40}\text{Ca}$ into the *pf*-shell isotopes.

It is interesting to notice that the *rp*-process is already active in the ^{40}Ca – ^{52}Fe region. This is because the double-magic ^{40}Ca is the natural end-point of the reactions during the minute long run up to the burst ignition where a small reaction flow is already present.

4.3.2. *Fig. 22:* $T = 6.90 \cdot 10^8 \text{K}$, $\rho = 9.35 \cdot 10^4 \text{g/cm}^3$, $X = 0.646$, $Y = 0.328$, $t = -8.600\text{s}$

Fig. 22 shows the maximum temperature during the convective phase occurring concurrently with the maximum temperature in the ignition region, which drives the superadiabatic temperature gradient responsible for the convective turnover. Higher temperatures are reached at this depth, but after this time, the region is no longer convective.

At the end of the convective phase, the (α, p) -process at the bottom of the convective region extends to ^{26}Si . Following that, the flow to heavier isotopes is impacted by the ^{30}S ($T_{1/2} = 1.10\text{s}$) waiting point. This is significant because the entire convective phase only lasts two half lives of ^{30}S . Similarly, there are bottlenecks at ^{59}Cu ($T_{1/2} = 91.9\text{s}$) and ^{60}Zn ($T_{1/2} = 5.28\text{m}$) which require a $^{60}\text{Zn}(p, \gamma) ^{61}\text{Ga}$ breakout that does not happen at these temperatures during the short convection phase.

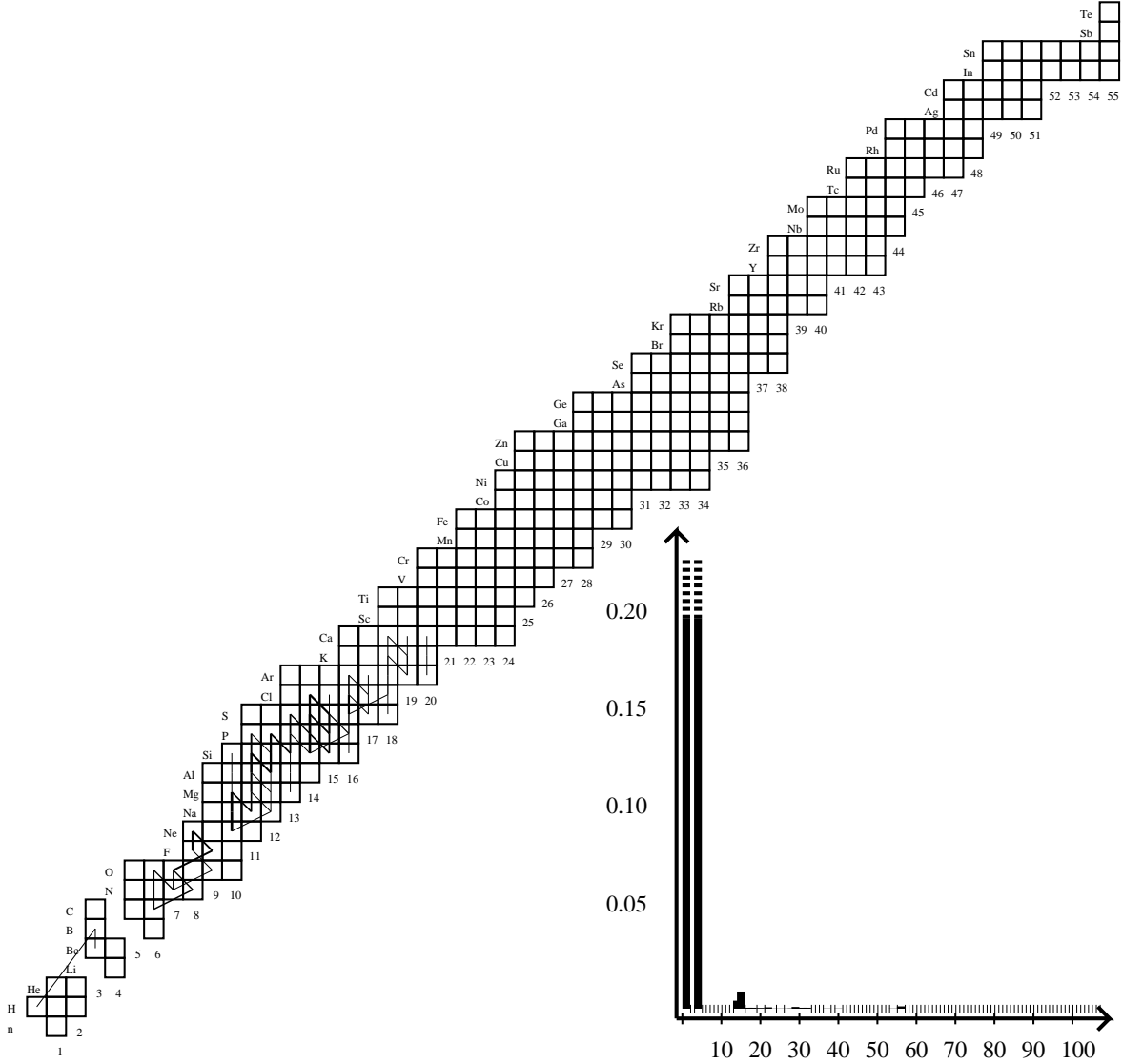


Fig. 22.— Convection region: $T = 6.90 \cdot 10^8 \text{K}$, $\rho = 9.35 \cdot 10^4 \text{g/cm}^3$, $X = 0.646$, $Y = 0.328$, $t = -8.600 \text{s}$. (see end of §4 for an explanation of the diagram).

4.4. Surface region

In H/He-ignited XRBs the convective region does not extend to the top of our model. This means that if the convective model does not severely underestimate the convective strength then heavier ashes are not brought to the surface. Since the matter at the top of our model is extremely opaque with mean free photon paths of $\sim 10^{-4}\text{cm}$, the photons are in local thermal equilibrium (LTE) and exhibit a black body spectrum with no lines. Comparison between the results of this section with observations therefore require this model to be coupled with a radiative transport code (see Weinberg et al. (2006)).

4.4.1. Fig. 23: $T = 5.31 \cdot 10^8\text{K}$, $\rho = 8.75 \cdot 10^3\text{g/cm}^3$, $X = 0.697$, $Y = 0.281$, $t = -0.209\text{s}$

The extent of the reaction flow at the maximum temperature is shown in Fig. 23 and ends at ^{56}Ni . This region is limited by $T < 5.3 \cdot 10^8\text{K}$ and the initial reactions are characterized by proton captures on the accreted heavy elements, which may have been destroyed by the surface impact (Bildsten et al. 1992).

4.5. Ocean (ashes)

The inner parts of the neutron star acts as a buffer absorbing heat from the burst. However, for this accretion rate it is radiated outwards again after the burst, therefore it does not heat the crust (Fujimoto et al. (1984)).

The early reaction flow which is caused by conductive heating in a hydrogen depleted environment is similar to the reaction flow in Fig. 10. Later it is characterized by residual helium, which has been advected down from the previous burst, capturing on alpha-chain nuclei extending to ^{36}Ar as shown in Fig. 24. Note that here we also have $^{12}\text{C}(p, \gamma)$ $^{13}\text{N}(\alpha, p)$ ^{16}O being much stronger than the direct $^{12}\text{C}(\alpha, \gamma)$ ^{16}O -reaction. Here the protons are supplied by many weak (α, p) -reactions on stable isotopes resulting from long lived β^+ -decays in the sulfur region in matter that has advected downwards from above.

5. Conclusion

Important in all the regions are the hot-CNO cycle and its respective breakout reactions, the (α, p) -process, as well as $(p, \gamma)(\gamma, p)$ -equilibria and waiting points of the rp -process. These are now discussed.

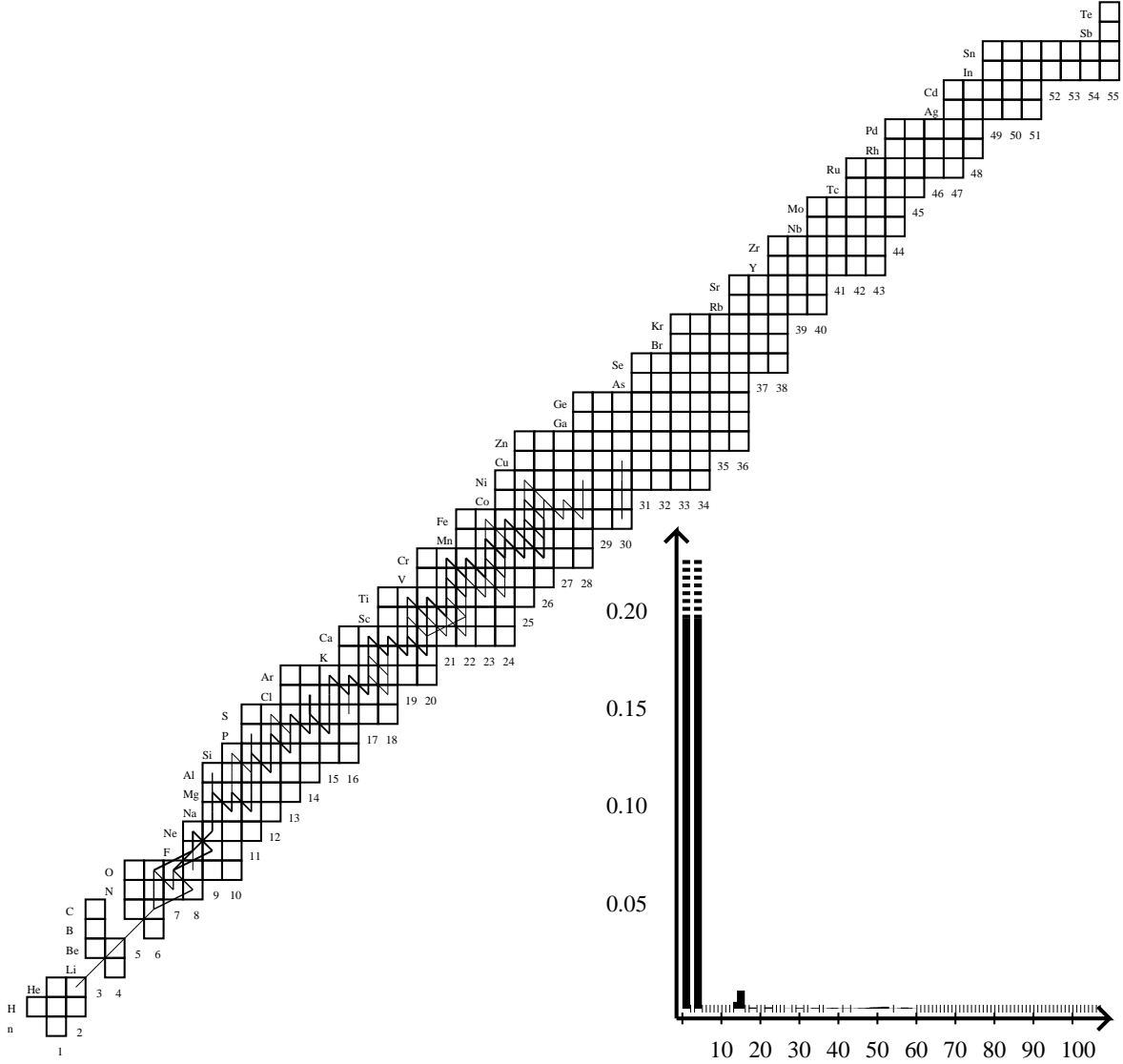


Fig. 23.— Surface: $T = 5.31 \cdot 10^8 \text{K}$, $\rho = 8.75 \cdot 10^3 \text{g/cm}^3$, $X = 0.697$, $Y = 0.281$, $t = -0.209 \text{s}$. (see end of §4 for an explanation of the diagram).

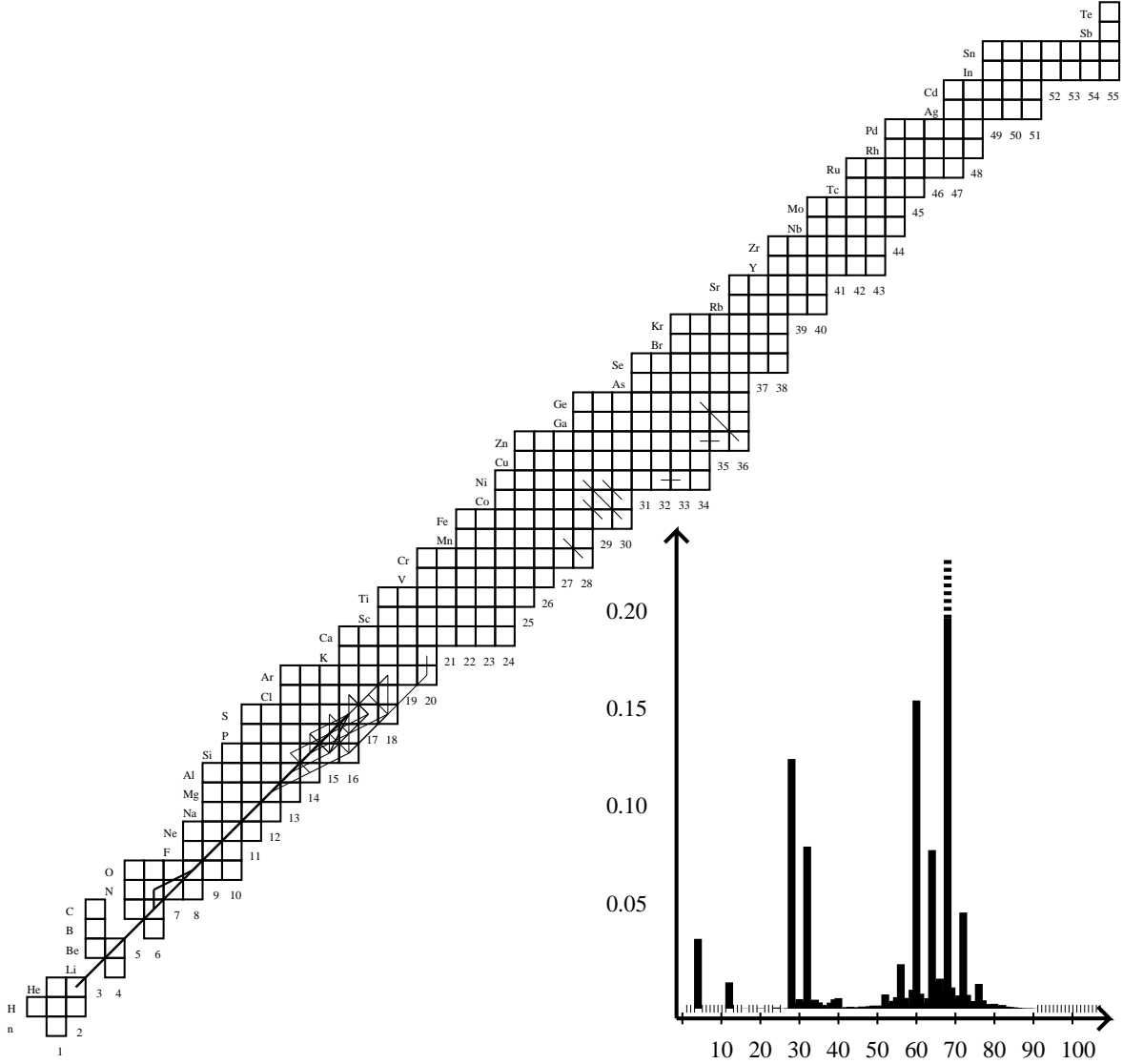


Fig. 24.— Ocean: $T = 9.55 \cdot 10^8 \text{K}$, $\rho = 6.06 \cdot 10^5 \text{g/cm}^3$, $X = 5.3 \cdot 10^{-11}$, $Y = 0.036$, $X_{68} = 0.22$, $t = -0.209 \text{s}$. (see end of §4 for an explanation of the diagram).

5.1. Hot CNO cycles

There are essentially three hot CNO cycles, specifically, the first hot CNO cycle: $^{12}\text{C}(p, \gamma) ^{13}\text{N}(p, \gamma) ^{14}\text{O}(\beta^+, \nu) ^{14}\text{N}(p, \gamma) ^{15}\text{O}(\beta^+, \nu) ^{15}\text{N}(p, \alpha) ^{12}\text{C}$, the second hot CNO cycle: $^{14}\text{O}(\alpha, p) ^{17}\text{F}(p, \gamma) ^{18}\text{Ne}(\beta^+, \nu) ^{18}\text{F}(p, \alpha) ^{15}\text{O}$ and third hot CNO cycle $^{15}\text{O}(\alpha, \gamma) ^{19}\text{Ne}(\beta^+, \nu) ^{19}\text{F}(p, \alpha) ^{16}\text{O}(p, \gamma) ^{17}\text{F}(p, \gamma) ^{18}\text{Ne}(\beta^+, \nu) ^{18}\text{F}(p, \alpha) ^{15}\text{O}$.

In order to activate the second hot CNO cycle, via $^{14}\text{O}(\alpha, p) ^{17}\text{F}$ and its breakout via $^{17}\text{F}(p, \gamma) ^{18}\text{Ne}(\alpha, p) ^{21}\text{Na}$, the third hot CNO cycle must activate hundreds of second prior to the runaway and achieve a breakout via $^{19}\text{Ne}(p, \gamma) ^{20}\text{Na}$. If the $^{15}\text{O}(\alpha, \gamma) ^{19}\text{Ne}$ -reaction is too weak, the third cycle never activates which means that the second cycle does not activate either and the thermonuclear runaway does not happen (Fisker et al. 2006). These rates are therefore quite significant in connecting the hot CNO cycle and the rp -process. Additionally, the reaction flow, in particular the third hot CNO cycle of Cooper & Narayan (2006), prior to the runaway is important for the ignition composition as it influences the concentration of hydrogen and helium which is important to the thermonuclear instability.

5.2. The (α, p) -process

The (α, p) -process is important because it is a temperature dependent process unlike the rp -process that contains temperature-independent β^+ -decays. The (α, p) -process therefore influences the characteristic timescale of the reaction flow up to $A = 36$ after which the Coulomb barrier becomes prohibitive. Furthermore, as shown in Fisker et al. (2004), the (α, p) -reactions in the (α, p) -process lie on waiting points with ^{30}S being the most significance. Other potential waiting points are ^{34}Ar and ^{26}Si .

The most important (α, p) -reactions for the XRB are therefore $^{26}\text{Si}(\alpha, p) ^{29}\text{P}$, $^{30}\text{S}(\alpha, p) ^{33}\text{Cl}$, and $^{34}\text{Ar}(\alpha, p) ^{37}\text{K}$. The $^{22}\text{Mg}(\alpha, p) ^{25}\text{Al}$ -reaction is most likely not as important, since the flow moves through the ^{22}Mg waiting point via $^{22}\text{Mg}(p, \gamma) ^{23}\text{Al}$ before the (α, p) -reaction becomes active.

Other (α, p) -reactions are less dominant since they operate at higher temperatures and on more proton-rich nuclei which are more susceptible to photodisintegration viz. $^{21}\text{Mg}(\alpha, p) ^{24}\text{Al}$, $^{24}\text{Si}(\alpha, p) ^{27}\text{P}$, $^{25}\text{Si}(\alpha, p) ^{28}\text{P}$, $^{28}\text{S}(\alpha, p) ^{31}\text{Cl}$, and $^{29}\text{S}(\alpha, p) ^{32}\text{Cl}$. The final (α, p) -reaction is $^{13}\text{N}(\alpha, p) ^{16}\text{O}$ which in the event of hydrogen depletion is stronger than the $^{12}\text{C}(\alpha, \gamma) ^{16}\text{O}$ reaction (also see Weinberg et al. (2006)).

5.3. The rp -process

The rp -process evolution depends on the concentration of hydrogen and the peak temperature. The peak temperature is easily estimated as $P = a_{rad}T^4$ which assumes that the pressure is fully supported by radiation and that the dynamical pressure is negligible. This is a good assumption as the gravitational binding energy is a factor ~ 20 – 50 higher than nuclear energy release of the burst. This dependence means that if the pressure of the ignition point is inaccurately determined, the peak temperature may be off by 10% or more which will significantly change the conclusions about the flow. Thermal and compositional inertia must be taken into account when considering the reaction flow. This was first shown by Woosley et al. (2004) who started with a pure ^{56}Fe atmosphere which allowed accreted matter to reach deeper layers. As a result Woosley et al. (2004) obtained the same results as the one-zone model of Schatz et al. (2001a) who based their ignition pressure and composition on analytical estimates. On the other hand, selfconsistently obtained bursts by Woosley et al. (2004) match the results obtained by other selfconsistent models (Rembges 1999; Fisker et al. 2003, 2004, 2005a,b) as well as this paper.

5.3.1. rp -process waiting points

Waiting points are isotopes from which further net reaction flows are (possibly temporarily) restricted due to either insufficiently high temperatures, insufficient capture particles, or the immediate photodisintegration due to a $(p, \gamma)(\gamma, p)$ -equilibrium. Waiting points are easily identified by their temporary abundance spikes. If a substantial, say 20% or more, part of the flow is backed up at a given isotope for a time comparable to the time scale of the XRB, it can significantly influence the shape of the observed luminosity curve (see Fisker et al. (2004)).

During the early build up to the XRB and during the early phases of the $^{21}\text{Mg}(p, \gamma)(\gamma, p)^{22}\text{Al}$ -equilibrium, which depends on the Q -value of the proton capture reaction, means that ^{21}Mg must β^+ -decay. The half life is short compared to the build-up phase which is on the order of hundreds of seconds. It is however comparable with the runaway time of the XRB. Therefore, the runaway depends on the $^{21}\text{Mg}(\alpha, p)^{24}\text{Al}$ reaction. Similar waiting points can be found along the (α, p) -process reaction path. They are ^{22}Mg , ^{26}Si , ^{30}S , ^{34}Ar , and ^{38}Ca . The dominant waiting point in this sequence depends on the extent of the (α, p) -process which depends on the peak temperature. If the peak temperature is extremely high e.g. $T_{peak} > 1.3 \times 10^9\text{K}$ these waiting points are bypassed by the (α, p) -process. For lower peak temperatures, these waiting point along with their associated Q -values and proton capture rates become important. However, our model has never reached peak temperatures above

$\sim 1.3 \times 10^9 \text{K}$ for accretion rates greater than $\dot{M} = 5 \cdot 10^{16} \text{ g s}^{-1}$ while accreting a solar composition (Anders & Grevesse 1989) on a self-consistently attained atmosphere. The ^{38}Ca waiting point might be circumvented by $^{38}\text{Ca}(p, \gamma) ^{39}\text{Sc}(p, \gamma) ^{40}\text{Ti}$ or $^{38}\text{Ca}(2p, \gamma) ^{40}\text{Ti}$.

Hot CNO-like cycles exist on well-bound isotopes such as ^{40}Ca . This isotope is particularly interesting since the flow passes through it during the quiescent phase. The low-temperature $^{43}\text{Sc}(p, \gamma) ^{44}\text{Ti}$ -reaction is therefore an important bottleneck as it determines the developing composition during the quiescent phase and thus the ignition conditions. The next bottleneck in the quiescent flow is $^{48}\text{Cr}(p, \gamma) ^{49}\text{Mn}$. During the burst (above $T \sim 5 \cdot 10^8 \text{K}$) the flow through the Ca-Ni region goes through many β^+ -decays and (p, γ) -reactions leaving no single determining reaction. Due to conservative scheme of numerical discretization of the model, it is possible to track minor variations in the luminosity due to individual rates.

The Ni-Se region provides several waiting points. The first waiting points are ^{59}Cu and ^{60}Zn . These half lives are on the order of the burst decay timescale and must be surpassed by proton captures in order for heavier isotopes to be produced. The latter is in $(p, \gamma)(\gamma, p)$ -equilibrium and thus depends on the Q -value of $^{60}\text{Zn}(p, \gamma) ^{61}\text{Ga}$. There is a possible flow via $^{61}\text{Ga}(p, \gamma) ^{62}\text{Ge}$. A similar situation exists on ^{64}Ge . Here ^{65}As is proton-unbound, so further flow depends on either a $2p$ -capture (Schatz et al. 1998) or a slow β^+ -decay. This is the reason why most of the flow stops at the $A = 64$. The atmosphere cools before a substantial amount of matter can decay and be processed to heavier isotopes. Similar situations exist on ^{68}Se , ^{72}Kr , ^{76}Sr , and ^{80}Zr where the corresponding ^{69}Br , ^{73}Rb , ^{77}Y , and ^{81}Nb are also proton-unbound. These waiting points have also been identified by Schatz et al. (1998) and by Woosley et al. (2004), who showed the significance of these decays by varying groups of electron capture and β^+ -decay rates up and down by 1 order of magnitude thus testing the impact of the efficiency of the reaction flow progression through the waiting points on the burst lightcurve.

5.4. Superbursts and convection

We showed that the peak burst temperature is less than $\sim 1.3 \text{GK}$ and thus not as high as previously assumed for nuclear reaction studies. This means that Te is not generated in quantity which corroborates previous multi-zone simulations of Fisker et al. (2003, 2005b); Woosley et al. (2004). The average mass of the ashes is ~ 64 (Fisker et al. 2003, 2005b; Woosley et al. 2004). At the same time carbon is slowly destroyed by helium captures below the ignition zone and at the top of the ocean. This corroborates the findings of Woosley et al. (2004) and it does not favor the parameter space requirements of current superburst theories (Cumming & Bildsten 2001). However, our model did not consider sedimentation effects

which may change this conclusion (Peng et al. 2006).

We find that the convective region does not hit the top of our model for mixed hydrogen/helium (sub-Eddington) bursters. Therefore we predict that any spectral lines observed during such bursts are not from material that was burned at any significant depth. However, at lower accretion rates, the convective region does hit the top of our model for helium bursters (see Fisker et al. (2005a)).

5.5. Summary

The main result of our calculations is the identification of the nuclear reaction sequences that power type I X-ray bursts. In particular, we describe the complete nuclear reaction flow as a function of time and depth, including branchings and waiting points, as it evolves with realistic, rapidly changing temperatures and densities. Clearly, the reaction sequences are more complex than previously assumed based on the analysis of much simpler models. Our work is a necessary first step towards identifying the critical nuclear reaction rates in X-ray bursts that have the largest impact on observables such as light curves, or, indirectly, the composition of the ashes. One can then also begin to disentangle the effects of nuclear burning on the luminosity (Fisker et al. 2004) from geometric effects such as the propagation of the burning front around the NS (Spitkovsky et al. 2002) to better explain the many different and somewhat inconsistent shapes of the burst luminosity profiles.

JLF and HS were supported by NSF-PFC grant PHY02-16783 through the Joint Institute of Nuclear Astrophysics². FKT and JLF acknowledge support from the Swiss NSF grant 20-068031.02.

REFERENCES

- Amthor, M., Galaviz, D., Heger, A., Sahkaruk, A., Schatz, H., & Smith, K. 2006, Proceedings of Science, NIC-IX, 68
- Anders, E. & Grevesse, M. 1989, *Geochim. Cosmochim. Acta*, 53, 197
- Ayasli, S. & Joss, P. C. 1982, *Astrophys. J.*, 256, 637

²see <http://www.JINAwab.org>

- Bildsten, L. 1998, in *The Many Faces of Neutron Stars*, ed. R. Buccheri, J. van Paradijs, & M. A. Alpar (Kluwer), 419
- Bildsten, L., Salpeter, E. E., & Wasserman, I. 1992, *Astrophys. J.*, 384, 143
- Brown, E. F. 2000, *Astrophys. J.*, 531, 988
- . 2003, Core code, private communication
- . 2004, *Astrophys. J. Lett.*, 614, 57
- Champagne, A. E. & Wiescher, M. 1992, *Ann. Rev. Nucl. Part. Sci.*, 42, 39
- Cooper, R. L. & Narayan, R. 2006, *Astrophys. J. Lett.*, 648, L123
- Cumming, A. & Bildsten, L. 2001, *Astrophys. J. Lett.*, 559, L127
- Fisker, J. L. 2004, PhD thesis, Univ. Basel
- Fisker, J. L., Brown, E., Liebendörfer, M., Schatz, H., & Thielemann, F.-K. 2005a, *Nucl. Phys.*, A758, 447
- Fisker, J. L., Brown, E., Liebendörfer, M., Thielemann, F.-K., & Wiescher, M. 2005b, *Nucl. Phys.*, A752, 604
- Fisker, J. L., Görres, J., Wiescher, M., & Davids, B. 2006, *Astrophys. J.*, 650, 332
- Fisker, J. L., Hix, W. R., Liebendörfer, M., & Thielemann, F.-K. 2003, *Nucl. Phys.*, A718, 614
- Fisker, J. L., Thielemann, F.-K., & Wiescher, M. 2004, *Astrophys. J. Lett.*, 608, L61
- Fryxell, B. A. & Woosley, S. E. 1982, *Astrophys. J.*, 261, 332
- Fujimoto, M. Y., Hanawa, T., & Miyaji, S. 1981, *Astrophys. J.*, 246, 267
- . 1984, *Astrophys. J.*, 278, 813
- Fujimoto, M. Y., Sztajno, M., Lewin, W. H. G., & van Paradijs, J. 1987, *Astrophys. J.*, 319, 902
- Fuller, G. M., Fowler, W. A., & Newman, M. J. 1980, *Astrophys. J. Suppl.*, 42, 447
- . 1982a, *Astrophys. J.*, 252, 715
- . 1982b, *Astrophys. J. Suppl.*, 48, 279

- Galloway, D. K., Cumming, A., Kuulkers, E., Bildsten, L., Chakrabarty, D., & Rotschild, R. E. 2004, *Astrophys. J.*, 601, 466
- Hanawa, T. & Fujimoto, M. Y. 1984, *Publ. Astron. Soc. Japan*, 36, 199
- Hanawa, T. & Sugimoto, D. 1983, *Publ. Astron. Soc. Japan*, 35, 491
- Hansen, C. J. & van Horn, H. M. 1975, *Astrophys. J.*, 195, 735
- Herndl, H., Jörres, Wiescher, M., Brown, B. A., & van Wormer, L. 1995, *Phys. Rev.*, C52, 1078
- Hix, W. R. & Thielemann, F.-K. 1999, *J. Comput. Appl. Math.*, 109, 321
- Iliadis, C., Endt, P. M., Prantzos, N., & Thompson, W. J. 1999, *Astrophys. J.*, 524, 434
- Joss, P. C. 1977, *Nature*, 270, 310
- . 1978, *Astrophys. J. Lett.*, 225, L123
- Joss, P. C. & Li, F. K. 1980, *Astrophys. J.*, 238, 287
- Käppeler, F., Thielemann, F.-K., & Wiescher, M. 1998, *Ann. Rev. Nucl. Part. Sci.*, 48, 175
- Koike, O., Hashimoto, M., Arai, K., & Wanajo, S. 1999, *Astron. Astrophys.*, 342, 464
- Langanke, K. & Martínez-Pinedo, G. 2001, *Nucl. Phys.*, A673, 481
- Liebendörfer, M., Rosswog, S., & Thielemann, F.-K. 2002, *Astrophys. J. Suppl.*, 141, 229
- Peng, F., Brown, E. F., & Truran, J. W. 2006, Sedimentation and type I X-ray bursts at low accretion rates, (astro-ph/0609583) submitted to *Astrophys. J.*
- Rembges, F. 1999, PhD thesis, University of Basel
- Rembges, F., Freiburghaus, C., Rauscher, T., Thielemann, F.-K., Schatz, H., & Wiescher, M. 1997, *Astrophys. J.*, 484, 412
- Roberts, L., Hix, W., Smith, M., & Fisker, J. 2006, *Proceedings of Science, NIC-IX*, 202
- Sakharuk, A., Elliot, T., Fisker, J. L., Hemingray, S., Kruizenga, A., Rauscher, T., Schatz, H., Smith, K., Thielemann, F.-K., & Wiescher, M. 2006, in *Capture Gamma-Ray Spectroscopy and Related Topics*, ed. A. Woehr & A. Aprahamian
- Schatz, H. 2002, *Acta. Phys. Pol. B*, 33, 227

- Schatz, H., Aprahamian, A., Barnard, V., Bildsten, L., Cumming, A., Ouellette, M., Rauscher, T., Thielemann, F.-K., & Wiescher, M. 2001a, *Phys. Rev. Lett.*, 86, 3471
- . 2001b, *Nucl. Phys.*, A688, 150
- Schatz, H., Aprahamian, A., Görres, J., Wiescher, M., Rauscher, T., Rembges, J. F., Thielemann, F.-K., Pfeiffer, B., Möller, P., Kratz, K. L., Herndl, H., Brown, B. A., & Rebel, H. 1998, *Phys. Rev.*, 294, 167
- Schatz, H., Bildsten, L., Cumming, A., & Wiescher, M. 1999, *Astrophys. J.*, 524, 1014
- Schatz, H. & Rehm, K. E. 2006, 777, 601
- Spitkovsky, A., Levin, Y., & Ushomirsky, G. 2002, *Astrophys. J.*, 566, 1018
- Strohmayer, T. E. & Bildsten, L. 2006, in *Compact Stellar X-ray Sources*, ed. W. H. G. Lewin & M. van der Klis (Cambridge University Press)
- Taam, R. E. 1980, *Astrophys. J.*, 241, 358
- . 1993, *Astrophys. J.*, 413, 324
- Taam, R. E. & Picklum, R. E. 1979, *Astrophys. J.*, 233, 327
- Thorne, K. S. 1977, *Astrophys. J.*, 212, 825
- van Wormer, L., Görres, J., Illiadis, C., Wiescher, M., & Thielemann, F.-K. 1994, *Astrophys. J.*, 423, 326
- Wallace, R. K. & Woosley, S. E. 1981, *Astrophys. J. Suppl.*, 45, 389
- Wallace, R. K., Woosley, S. E., & Weaver, T. A. 1982, *Astrophys. J.*, 258, 696
- Weinberg, N., Bildsten, L., & Schatz, H. 2006, *Astrophys. J.*, 639, 1018
- Weiss, A., Hillebrandt, W., Thomas, H.-C., & Ritter, H. 2004, *Cox & Giuli's Principles of Stellar Structure* (Cambridge, UK: Cambridge Scientific Publishers)
- Wiescher, M. 2001, *Nucl. Phys.*, A688, 241
- Wiescher, M. & Görres, J. 1989, *Astrophys. J.*, 346, 1041
- Wiescher, M., Görres, J., Graff, S., Buchmann, L., & Thielemann, F.-K. 1989, *Astrophys. J.*, 343, 352

Wiescher, M. & Schatz, H. 2001, Nucl. Phys., A693, 269

Woosley, S. E., Heger, A., Cumming, A., Hoffman, R. D., Pruet, J., Rauscher, T., Fisker, J. L., Schatz, H., Brown, B. A., & Wiescher, M. 2004, Astrophys. J. Suppl., 151, 75

Woosley, S. E. & Taam, R. E. 1976, Nature, 263, 101